STRESS, RIGIDITY AND SEDIMENT STRENGTH CONTROL MEGATHRUST EARTHQUAKE AND TSUNAMI DYNAMICS

PREPRINT, COMPILED APRIL 15, 2021

Thomas Ulrich,[1*] **Alice-Agnes Gabriel,**[1] **Elizabeth H. Madden**[2]

[1]Department of Earth and Environmental Sciences,
Ludwig-Maximilians-Universität München, Munich, Germany
[2] Observatório Sismológico, Instituto de Geociências,
Universidade de Brasília, Brasília, Brazil

[*]E-mail: ulrich@geophysik.uni-muenchen.de

Megathrust faults host the largest earthquakes on Earth which can trigger cascading hazards such as devastating tsunamis. Determining characteristics that control subduction zone earthquake and tsunami dynamics is critical to mitigate megathrust hazards, but is impeded by structural complexity, large spatio-temporal scales, and scarce or asymmetric instrumental coverage. Here we use high-performance computing multi-physics simulations to show that tsunamigenesis and earthquake dynamics are controlled by along-arc variability in regional tectonic stresses together with depth-dependent variations in rigidity and yield strength of near-fault sediments. We aim to identify dominant regional factors controlling megathrust hazards. To this end, we demonstrate how to unify and verify the required initial conditions for geometrically complex, multi-physics earthquake-tsunami modeling from interdisciplinary geophysical observations. We present large-scale computational models of the 2004 Sumatra-Andaman earthquake and Indian Ocean tsunami that reconcile near- and far-field seismic, geodetic, geological, and tsunami observations and reveal tsunamigenic trade-offs between slip to the trench, splay faulting, and bulk yielding of the accretionary wedge. Our computational capabilities render possible the incorporation of present and emerging high-resolution observations into dynamic-rupture-tsunami models and will be applicable to other large megathrust earthquakes. Our findings highlight the importance of regional-scale structural heterogeneity to decipher megathrust hazards.

Variations in megathrust earthquake rupture behaviour are associated with tectonic, mechanical and structural factors highlighting the importance of depth-dependent and along-arc subduction zone heterogeneity (*1*–*5*). Large tsunamis may be caused by various co-seismic mechanisms including large slip to the trench, as observed during the 2011 Tohoku earthquake (*6*) and inferred from tsunami deposits along the Kuril trench (*7*), slip on splay faults (*8*), and inelastic co-seismic deformation generating significant uplift near the trench (*9, 10*).

Here, we hypothesize that a few regional scale subduction zone characteristics control earthquake kinematics, earthquake dynamics, and tsunami genesis. These characteristics include rock rigidity and yield strength, plate convergence rate, and regional tectonic stresses. Such features and their heterogeneities can be readily constrained by seismic, geodetic, and geological observations (e.g. (*11*)).

The 2004 M_w 9.1 to 9.3 Sumatra-Andaman earthquake and subsequent Indian Ocean tsunami initiated a new era of geophysical studies focused on deciphering the complex source characteristics of large subduction zone earthquakes and how these relate to tsunami generation. The earthquake's unexpectedly large moment magnitude challenged the idea that convergence rate and age of the oceanic lithosphere control the largest earthquakes on subduction interfaces (e.g., (*12–14*)). The Andaman trench involves a middle-aged oceanic lithosphere, aged 50-70 million years, (*15*), converging at relatively slow rate as low as 20 mm/year in the Northern Andaman section (*16*) and historically it only hosted thrust earthquakes of less than M 7.9 (see Fig. 1a). Then, the 2004 dynamically complex rupture ripped 1300–1500 km of faults along the trench for 8–10 minutes and challenged data-driven analyses. Inversion of seismic and geodetic data (*17–19*) are complemented by less conventional data inferences, including normal modes (*20*), multiple centroid moment tensor (CMT) inversions (*21*), gravity (e.g., (*22*)), tsunami (e.g., (*23*)) or hydroacoustic waves (e.g., (*24*)), and seismic arrays (*25*). Nonetheless, data-driven source models include large variations (*26*) and produce synthetic tsunamis in varying agreement with satellite or inundation records (*27*). Furthermore, the earthquake generated a tsunami up to 30 meters high in Northern Sumatra (*28*), which seems at odds with slip on the shallowly dipping subduction interface. Slip on several splay faults during or soon after the megathrust event was inferred from seafloor mapping (*29–31*), tsunami modeling (*32*) and aftershock relocation (*33*). Alternatively, near-trench slip in lithified sediments at the southern end of the rupture may be responsible for the tsunami (*34–38*).

Rising computational resources and efficiency now allow data-integrated dynamic rupture modeling of crustal earthquakes that complements data-driven analyses. Dynamic rupture models provide physically self-consistent descriptions of how faults yield and slide, while their non-linearity and complexity limit the total number of feasible numerical experiments. These methods have unraveled complex and/or poorly instrumented events in various tectonic contexts (e.g., (*39–44*)). However, constraining the dynamics and extracting hazard implications from 3D dynamic models of megathrust earthquakes requires new methods that assimilate distinct data and inferences.

We here introduce a stringent forward modeling approach to evaluate the key-factors controlling earthquake-tsunami behavior. Large-scale dynamic rupture modeling provides a bridge between scales harnessing the ability to uncover the physical mechanisms and parameters relevant to the co-seismic rupture of naturally complex fault networks comprising megathrusts. We connect subduction mechanics with a scenario of the 2004 Sumatra-Andaman earthquake and tsunami produced by a physics-based computational model. Evaluation against independent observations in the near- and far-field ensures that the scenario captures the key observed earthquake characteristics (magnitude, moment release, focal mechanism(s), rupture duration, teleseismic waveforms, and ground displacements) and main characteristics of the Indian Ocean tsunami. The model reveals that the interplay of a curved megathrust geometry with the along-arc variability of regional tectonic loading and plate convergence rates, and strong rigidity variations with depth near the megathrust interface, are dominant factors controlling the earthquake. We then analyze a major conundrum (*45*) of earthquake-tsunami interaction that is ill-constrained by observational data: the interplay of near-trench earthquake dynamics and sedimentary yielding controlling tsunami generation and propagation. We present two additional scenarios with alternative near-trench sedimentary rock strength. These demonstrate that the strength of trench sediments and the associated changes to on-fault megathrust and splay fault slip versus off-fault plastic yielding control the seafloor displacements and, in turn, the tsunami.

To model earthquake dynamics, choices about the preexisting state of stress and the friction law governing fault strength and sliding, as well as the lithological structure and fault geometries, are required. We constrain all required initial conditions on subduction zone scale and specific to the Sumatra-Andaman trench. Regional principal stress orientations from stress inversion are aligned with geodetic observations and combined with seismo-tectonic observations and the Mohr-Coulomb failure theory to constrain principal prestress magnitudes and fault friction parameters (Fig. 1a and Methods Sec. “Principal stress orientations and magnitudes”). We account for along-arc variations in convergence rate and assume over-pressurized fault fluids (Fig. 1b). Without regional prestress variation, rupture fails to stop dynamically at the northernmost megathrust, and slip larger than 40 m accumulates there (Fig. E7a and Methods Sec. “The importance of convergence-rate modulated regional driving stresses”). Horizontal ground displacements then exceed observations by factors of 2 to 5 (Fig. E7b). Inferences of principal stress rotations after megathrust earthquakes provide direct information about the ratio of stress drop over prestress (*4*). We propose to constrain the co-seismic frictional strength drop on the megathrust based on stress rotation observations (see Fig. 1c and Methods Sec. “Co-seismic stress rotation to constrain fault friction”). The 3D structural model (Fig. 1d and Methods Sec. “Regional lithological structure” and “Fault geometry”) accounts for strong rigidity variations with depth in the near-fault region (Fig. 1e and Methods Sec. “Regional lithological structure”), bathymetry and topography, and a complex, embedded fault network consisting of the curved megathrust and three splay faults, a backthrust and two forethrusts splaying off of it. All faults intersect each other and the ocean floor, with megathrust-bathymetry intersection angles as low as 30° (*46*). We find that the following initial conditions are required to produce a realistic earthquake-tsunami scenario of the 2004 event: a non-Andersonian prestress state with pronounced along-arc and depth-dependent variations, near-lithostatic fluid pressure that results in low effective normal stress near the megathrust, strong frictional weakening, a 3D velocity structure specifically accounting for the low rigidities at shallow depth within the subduction channel (Methods Sec. "The importance of strongly depth-dependent rigidity"), and sediments of high yield strength.

Regional variation of tectonic driving stresses modulated by convergence rates and the geometry of the slab and splay faults explains first-order static earthquake characteristics, such as geodetic displacements at regional distance. Along-depth variation in rock rigidity and yield strength of near-trench sediments determine rupture dynamics, such as rupture speed, as well as coseismic uplift, and, thus, tsunami generation.

Fig. 2a shows the rupture evolution of the observationally constrained dynamic earthquake scenario of the 2004 Sumatra event. Complex rupture dynamics evolve across 1300 km of the fault system, including dynamic rupture transfers to both backthrusts and the forethrust. Along-depth variation in rock rigidity leads to faster rupture at depth and slower rupture at the trench yielding the boomerang-shaped slip pulse apparent in Fig. 2a. This pulse consists of multiple rupture fronts, which are caused by reflected waves and head waves generated at structural interfaces and the complex free surface.

Along-arc variations in convergence rates do significantly modulate earthquake evolution. These translate into modulations of stress drop and fault slip. In the hypocentral region, the subduction interface is nearly optimally oriented. While rupture is forced to initiate (Supplementary information Sec. "Earthquake nucleation"), locally decreased prestress reproduces spontaneous arrest immediately to the south of the hypocenter. The rupture also arrests spontaneously to the north, where lower convergence rates yield a critically lower prestress.

Our modeling insights are strengthened by the scenario's agreement with the main source characteristics of the 2004 earthquake. Its moment magnitude of $M_\mathrm{w} = 9.2$ falls in the range of inferred estimates (M_w 9.1 to 9.3, (*26*)). The synthetic focal mechanism, with strike/dip/rake angles of 343°/10°/114° (Fig. 2b) is compatible with the respective observational inferences of 336°/7°/114° by USGS. The synthetic moment rate release resembles available source time functions inferred from teleseismic data (*17*)(Fig. 2c). The scenario is also in excellent agreement with all five focal mechanisms of the multi-CMT teleseismic inversion by (*21*) (Fig. 2b). In Supplementary information Sec. "Multiple point source analysis: source time functions", we detail the derivation of equivalent multiple moment tensors and source time functions from dynamic rupture models. The scenario also reproduces the timing, amplitudes and envelopes of recorded long-period teleseismic waveforms (Fig. E3a at nine stations (Fig. E3b) at periods of 150 s to 500 s with an average rRMS of 0.7 (see Methods Sec. "Teleseismic model validation")).

Figure 3 shows the rupture speed and slip characteristics along the megathrust from the dynamic rupture scenario. The speed of the modeled rupture front is slower than the S-wave speed of the host rocks (Fig 3a) everywhere. Shallow supershear rupture is prevented by off-fault plastic yielding. Rupture speed strongly varies along-depth due to the incorporated rigidity variations (Fig. 1e). The average speed resembles observational Rayleigh wave (*47*) and acoustic (*48*) inferences including along-arc variations (Fig. 2d). The scenario captures changes in rake along megathrust strike, from thrusting in the south to increasingly oblique faulting farther north (Fig. 3b). This variation follows the change in the strike of the non-planar megathrust relative to the laterally varying regional loading.

The dynamic rupture scenario yields a smooth fault slip distribution with along-arc variations (Fig. 3c). Regions of high slip at the trench alternate with flatter portions of the shallow interface that experience less slip. Synthetic fault slip agrees in terms of along-arc and along-depth distribution to first order with data-driven kinematic models (Fig. 3d,e).

Near-field and far-field horizontal and vertical ground displacements reproduce observations (Figs. 2e,f and E1) in terms of amplitude and orientation. We denote deviations to spatial and temporal model limitations. The dynamic scenario does not account for Earth curvature, small-scale 3D crustal structure in the far-field, nor the contribution of after-slip. Near-field synthetics may be affected by the simplistic treatment of earthquake nucleation and arrest in our model.

All three splay faults incorporated in the model are dynamically activated (Fig. 2a) and cause a noticeable signature in uplift and subsidence (Fig. 2f). The splays host significantly less slip (6–8 m) than the subduction interface (up to 25 m), however, slip efficiently transfers into vertical uplift due to their steeper dip. The total contribution of splay fault slip to vertical uplift remains limited in spatial extent and amplitude.

While outer-rise aftershock sequences help to constrain the extent of slip to the trench during megathrust ruptures (*49*), the balance between shallow slip and off-fault yielding remains elusive from geodetic and seismic observations. However, both effects have been shown to impact vertical uplift (*45, 50*) and therefore may influence tsunami behavior. To address this, we model tsunami genesis and propagation sourced by dynamic earthquake rupture as detailed in Methods Sec. "Tsunami modeling". Synthetic tsunamis are generated from the time-dependent horizontal and vertical coseismic seafloor displacements.

Relative to the dynamic-rupture scenario described previously, we vary the yield strength of near-trench sediments in two alternative dynamic scenarios with weaker and stronger near-trench sediments, yielding respectively more or less off-fault deformation (see Fig. 4a).Cohesion and bulk friction depend on local mineralogy and lithology, depth, fluid pressure, stress orientation and magnitude and the respective damage level of the host rock within and beyond the subduction channel. In all models, the bulk cohesion is a combination of a depth-dependent term, $C_1(z)\sigma'_c$ with σ'_c the effective confining stress, which accounts for rock strengthening with depth, and a constant term C_0, which controls localization of off-fault yielding at shallow depth, as detailed in Methods Sec. "Off-fault plasticity"). Mineralogical and lithological specific laboratory measurements of cohesion and its dependence on confining stress are challenging and may reveal strong local heterogeneity (*51*). For simplicity, in the base dynamic-rupture-tsunami scenario, we assign $C_0 = 1$ MPa and $C_1(z) = 1$, appropriate for partially consolidated sediments (*35*). Slip to the trench (Fig. 4b) is limited by asymmetric, wide-spread plastic yielding in the shallow part of the accretionary wedge (Fig. 4a). The alternative scenarios result in distinctly different distributions of shallow slip in the upper 15 km (Fig. 4b). Stronger sediments ($C_0 = 10$ MPa and $C_1(z) = 1$ representing lithified sediments entering the trench) cause localized and weak off-fault yielding and fault slip locally exceeds 30 m at the trench. In contrast, weaker sediments ($C_0 = 0.3$ MPa, $C_1(z) = \max(1, (z/18000)^2)$ and at shallow depth decreased bulk internal friction, representing unconsolidated sediments) prevent near-trench slip, but cause widespread plastic deformation off the megathrust and off the splay faults (see Fig. E2d). Also, the shallow rupture speed in the uppermost 10 km of this scenario (Fig. E8a,b) is reduced, averaging only 0.5 km/s, which is close to the characteristic slow speed of tsunami-earthquakes (*52*).

While all three scenarios vary near the trench, they yield indistinguishable teleseismic (Fig. E3) and comparable geodetic synthetics (Fig. E2). They also are equivalent in terms of macroscopic earthquake kinematics (Fig. E8c), however, rupture duration is 100 s shorter for the strong sediment scenario compared to the base scenario. The radiation efficiency of the flat, shallow parts of the megathrust is low in all scenarios.

We evaluate the dynamic-rupture-tsunami scenarios against geodetic tsunami observations. All three dynamic rupture scenarios source a large-scale tsunami that propagates across the entire simulated domain (see Fig. 4c). The amplitudes and shorter period characteristics of the dynamically sourced tsunami synthetics are sensitive to both fault slip at the trench and off-fault plastic deformation. The tsunami sourced by the base scenario and the stronger-sediment scenario match timing and amplitude of water height anomalies captured by the Jason-1 satellite about 2 hours after the mainshock (see Fig. 4d). The tsunami sourced by the weaker-sediment earthquake scenario featuring pronounced off-fault yielding and no slip to the trench produces tsunami waves amplified by a factor of 2.

All three scenarios capture the pronounced two-peak characteristic of the first tsunami wave, a feature that is recovered by few of the kinematic models in (*27*). However, the overall better agreement of the base and stronger sediment scenarios reconciles previous stochastic analysis (*38*) implying that surface faulting in the southern rupture zone best reproduces the double-peak in the altimetry data and is consistent with the inference of lithified sediment in this region (*37, 53*).

We identify key factors controlling megathrust earthquake dynamics and tsunamigenic potential using multi-physics numerical modeling capable of incorporating sophisticated imaging of complex lithological and fault structure in combination with a stringent framework to determine earthquake initial conditions. The such-found conditions governing a geometrically complex model of the 2004 Sumatra-Andaman earthquake and Indian Ocean tsunami include elevated fluid pressure and reveal a high friction drop on a statically strong and well-oriented megathrust interface. A simple linear-slip weakening friction law combined with off-fault yielding captures key features of the seismic, geodetic, and tsunami observations in the near- and far-field.

Natural megathrusts vary in additional ways due to local complexities in slab morphology and convergence rates, as well as sediment cover. Our approach yields smoothly varying rupture dynamics and kinematic characteristics, such as fault slip and rupture speed, across the megathrust. While spatial variations in geometric and rheological complexities are found to correlate on length scales of hundreds of meters in 3D imaging (*11*), smaller-scale geometrical complexity of the fault interfaces may produce more heterogeneity in these features, as inferred in some data-driven kinematic models. The subduction interface remains nearly optimally oriented in this model (see Fig. E9) and the variation of absolute prestress magnitudes is small. The variations in regional scale megathrust geometry are counteracted by the observationally constrained variations in the regional driving stresses. This approach can be extended to include further sources of spatio-temporal heterogeneities, which may modulate prestress and thus megathrust rupture dynamics. This can include variations in seismic coupling (*54, 55*), subducted structural features (*56*), as well as stress changes due to aseismic creep and previous earthquakes (*57, 58*).

Both sediment load entering the subduction channel and lithification of those sediments have been connected to the near-surface behavior and tsunamigenic potential of subduction zones. While high sedimentation has been linked statistically to large earthquakes (*59–62*), the scenarios we present here emphasize that the strength of these sediments is key. Indeed, we find that depth-dependent rigidity and the amount of off-fault plastic yielding of near-trench rocks are dominant factors controlling earthquake dynamics and tsunami genesis. Specifically, the Bengal fan to the north is associated with increased sediment thickness (*63, 64*) and a thick layer of lithified sediment has been evidenced in the southern part of the Andaman trench (*53*). However, the nature and amount of sediments certainly vary along the megathrust. We expect that taking along-arc variations of rigidity and sediment yield strength into account will lead to along-arc variations in shallow rupture dynamics and tsunami genesis (*45*).

The physics-based numerical models presented here reveal relationships between megathrust fault geometries, tectonic loading, rigidity variations with depth and sediment strength with megathrust hazard, and emphasize the importance of regional-scale structural heterogeneity for earthquake dynamics and tsunami genesis. Novel seafloor observatories (*65*) have the potential to provide detailed images of near-trench regions world-wide. Our computational capabilities render possible the incorporation of present and emerging high-resolution observations into dynamic-rupture-tsunami models. We have demonstrated for the Great Sumatra-Andaman earthquake and tsunami that dominant factors controlling megathrust hazards can be identified, which, in principle can be applied to subduction zones globally. Incorporating smaller scale heterogeneities and observational uncertainties into our models will enhance both scenario focused modeling and physics-based probabilistic hazard assessment of the future.

REFERENCES

1. Bilek, S. L. & Lay, T. Rigidity variations with depth along interplate megathrust faults in subduction zones. *Nature* **400**, 443–446 (1999).
2. Tobin, H. J. & Saffer, D. M. Elevated fluid pressure and extreme mechanical weakness of a plate boundary thrust, Nankai Trough subduction zone. *Geology* **37**, 679–682 (2009).
3. Noda, H. & Lapusta, N. Stable creeping fault segments can become destructive as a result of dynamic weakening. *Nature* **493**, 518–521 (2013).
4. Hardebeck, J. L. Stress orientations in subduction zones and the strength of subduction megathrust faults. *Science* **349**, 1213–1216 (2015).
5. Sallarès, V. & Ranero, C. R. Upper-plate rigidity determines depth-varying rupture behaviour of megathrust earthquakes. *Nature* **576**, 96–101 (2019).
6. Fujiwara, T. *et al.* The 2011 Tohoku-Oki Earthquake: Displacement Reaching the Trench Axis. *Science* **334**, 1240–1240 (2011).
7. Nanayama, F. *et al.* Unusually large earthquakes inferred from tsunami deposits along the Kuril trench. *Nature* **424**, 660–663 (2003).

8. Cummins, P. R. & Kaneda, Y. Possible splay fault slip during the 1946 Nankai earthquake. *Geophysical Research Letters* **27**, 2725–2728 (2000).
9. Lay, T. *et al.* Depth-varying rupture properties of subduction zone megathrust faults. *Journal of Geophysical Research: Solid Earth* **117** (2012).
10. Seno, T. The 21 September, 1999 Chi-Chi Earthquake in Taiwan: Implications for Tsunami Earthquakes. *Terrestrial, Atmospheric and Oceanic Sciences* **11**, 701 (2000).
11. Kirkpatrick, J. D. *et al.* Subduction megathrust heterogeneity characterized from 3D seismic data. *Nature Geoscience* **13**, 369–374 (2020).
12. Ruff, L. & Kanamori, H. Seismicity and the subduction process. *Physics of the Earth and Planetary interiors* **23**, 240–252 (1980).
13. Rikitake, T. Recurrence of great earthquakes at subduction zones. *Tectonophysics* **35**, 335–362 (1976).
14. Uyeda, S. & Kanamori, H. Back-arc opening and the mode of subduction. *Journal of Geophysical Research: Solid Earth* **84**, 1049–1061 (1979).
15. Müller, R. D., Roest, W. R., Royer, J.-Y., Gahagan, L. M. & Sclater, J. G. Digital isochrons of the world's ocean floor. *Journal of Geophysical Research: Solid Earth* **102**, 3211–3214 (1997).
16. Curray, J. R. Tectonics and history of the Andaman Sea region. *Journal of Asian Earth Sciences* **25**, 187–232 (2005).
17. Ammon, C. J. *et al.* Rupture Process of the 2004 Sumatra-Andaman Earthquake. *Science* **308**, 1133–1139 (2005).
18. Chlieh, M. *et al.* Coseismic Slip and Afterslip of the Great Mw 9.15 Sumatra–Andaman Earthquake of 2004. *Bulletin of the Seismological Society of America* **97**, S152–S173 (2007).
19. Rhie, J., Dreger, D., Bürgmann, R. & Romanowicz, B. Slip of the 2004 Sumatra–Andaman Earthquake from Joint Inversion of Long-Period Global Seismic Waveforms and gps Static Offsets. *Bulletin of the Seismological Society of America* **97**, S115–S127 (2007).
20. Stein, S. & Okal, E. A. Speed and size of the Sumatra earthquake. *Nature* **434**, 581–582 (2005).
21. Tsai, V. C., Nettles, M., Ekström, G. & Dziewonski, A. M. Multiple CMT source analysis of the 2004 Sumatra earthquake. *Geophysical Research Letters* **32** (2005).

22. de Linage, C. *et al.* Separation of coseismic and postseismic gravity changes for the 2004 Sumatra-Andaman earthquake from 4.6 yr of GRACE observations and modelling of the coseismic change by normal-modes summation. *Geophysical Journal International* **176**, 695–714 (2009).

23. Fujii, Y. & Satake, K. Tsunami Source of the 2004 Sumatra-Andaman Earthquake Inferred from Tide Gauge and Satellite Data. *Bulletin of the Seismological Society of America* **97**, S192–S207 (2007).

24. de Groot-Hedlin, C. D. Estimation of the rupture length and velocity of the Great Sumatra earthquake of Dec 26, 2004 using hydroacoustic signals. *Geophysical Research Letters* **32**, L11303 (2005).

25. Ishii, M., Shearer, P. M., Houston, H. & Vidale, J. E. Extent, duration and speed of the 2004 Sumatra–Andaman earthquake imaged by the Hi-Net array. *Nature* **435**, 933 (2005).

26. Shearer, P. & Bürgmann, R. Lessons learned from the 2004 Sumatra-Andaman megathrust rupture. *Annual Review of Earth and Planetary Sciences* **38**, 103–131 (2010).

27. Poisson, B., Oliveros, C. & Pedreros, R. Is there a best source model of the Sumatra 2004 earthquake for simulating the consecutive tsunami? *Geophysical Journal International* **185**, 1365–1378 (2011).

28. Borrero, J. C. Field Data and Satellite Imagery of Tsunami Effects in Banda Aceh. *Science* **308**, 1596–1596 (2005).

29. Sibuet, J. *et al.* 26th December 2004 great Sumatra–Andaman earthquake: Co-seismic and post-seismic motions in northern Sumatra. *Earth and Planetary Science Letters* **263**, 88–103 (2007).

30. Chauhan, A. P. S. *et al.* Seismic imaging of forearc backthrusts at northern Sumatra subduction zone. *Geophysical Journal International* **179**, 1772–1780 (2009).

31. Singh, S. C. *et al.* Seismic evidence for broken oceanic crust in the 2004 Sumatra earthquake epicentral region. *Nature Geoscience* **1**, 777–781 (2008).

32. DeDontney, N. & Rice, J. R. Tsunami Wave Analysis and Possibility of Splay Fault Rupture During the 2004 Indian Ocean Earthquake. *Pure and Applied Geophysics* **169**, 1707–1735 (2012).

33. Waldhauser, F., Schaff, D. P., Diehl, T. & Engdahl, E. R. Splay faults imaged by fluid-driven aftershocks of the 2004 Mw 9.2 Sumatra-Andaman earthquake. *Geology* **40**, 243–246 (2012).

34. Geersen, J., McNeill, L., Henstock, T. J. & Gaedicke, C. The 2004 Aceh-Andaman Earthquake: Early clay dehydration controls shallow seismic rupture: Shallow Rupture off Northern Sumatra. *Geochemistry, Geophysics, Geosystems* **14**, 3315–3323 (2013).

35. Gulick, S. P. S. *et al.* Updip rupture of the 2004 Sumatra earthquake extended by thick indurated sediments. *Nature Geoscience* **4**, 453–456 (2011).

36. Qin, Y. & Singh, S. C. Seismic evidence of a two-layer lithospheric deformation in the Indian Ocean. *Nature Communications* **6**, 8298 (2015).

37. Hüpers, A. *et al.* Release of mineral-bound water prior to subduction tied to shallow seismogenic slip off Sumatra. *Science* **356**, 841–844 (2017).

38. Geist, E. L., Titov, V. V., Arcas, D., Pollitz, F. F. & Bilek, S. L. Implications of the 26 December 2004 Sumatra-Andaman Earthquake on Tsunami Forecast and Assessment Models for Great Subduction-Zone Earthquakes. *Bulletin of the Seismological Society of America* **97**, S249–S270 (2007).

39. Olsen, K. B., Madariaga, R. & Archuleta, R. J. Three-Dimensional Dynamic Simulation of the 1992 Landers Earthquake. *Science* **278**, 834–838 (1997).

40. Douilly, R., Aochi, H., Calais, E. & Freed, A. M. Three-dimensional dynamic rupture simulations across interacting faults: The Mw7.0, 2010, Haiti earthquake. *Journal of Geophysical Research: Solid Earth* **120**, 1108–1128 (2015).

41. Kyriakopoulos, C., Oglesby, D. D., Funning, G. J. & Ryan, K. J. Dynamic Rupture Modeling of the *M* 7.2 2010 El Mayor-Cucapah Earthquake: Comparison With a Geodetic Model. *Journal of Geophysical Research: Solid Earth* **122**, 10,263–10,279 (2017).

42. Wollherr, S., Gabriel, A.-A. & Mai, P. M. Landers 1992 "Reloaded": Integrative Dynamic Earthquake Rupture Modeling. *Journal of Geophysical Research: Solid Earth* **124**, 6666–6702 (2019).

43. Ulrich, T., Gabriel, A.-A., Ampuero, J.-P. & Xu, W. Dynamic viability of the 2016 Mw 7.8 Kaikōura earthquake cascade on weak crustal faults. *Nature Communications* **10**, 1213 (2019).

44. Ulrich, T. *et al.* Coupled, Physics-Based Modeling Reveals Earthquake Displacements are Critical to the 2018 Palu, Sulawesi Tsunami. *Pure and Applied Geophysics* **176**, 4069–4109 (2019).

45. Ma, S. & Nie, S. Dynamic Wedge Failure and Along-Arc Variations of Tsunamigenesis in the Japan Trench Margin. *Geophysical Research Letters* **46**, 8782–8790 (2019).

46. Moore, G. F. *et al.* Three-Dimensional Splay Fault Geometry and Implications for Tsunami Generation. *Science* **318**, 1128–1131 (2007).

47. Vallee, M. Rupture Properties of the Giant Sumatra Earthquake Imaged by Empirical Green's Function Analysis. *Bulletin of the Seismological Society of America* **97**, S103–S114 (2007).

48. Guilbert, J. Use of hydroacoustic and seismic arrays to observe rupture propagation and source extent of the $M_w = 9.0$ Sumatra earthquake. *Geophysical Research Letters* **32**, L15310 (2005).

49. Sladen, A. & Trevisan, J. Shallow megathrust earthquake ruptures betrayed by their outer-trench aftershocks signature. *Earth and Planetary Science Letters* **483**, 105–113 (2018).

50. Kozdon, J. E. & Dunham, E. M. Rupture to the Trench: Dynamic Rupture Simulations of the 11 March 2011 Tohoku Earthquake. *Bulletin of the Seismological Society of America* **103**, 1275–1289 (2013).

51. Brodsky, E. E. *et al.* The postearthquake stress state on the Tohoku megathrust as constrained by reanalysis of the JFAST breakout data: JFAST Breakouts. *Geophysical Research Letters* **44**, 8294–8302 (2017).

52. Kanamori, H. Mechanism of tsunami earthquakes. *Physics of the Earth and Planetary Interiors* **6**, 346–359 (1972).

53. Qin, Y. & Singh, S. C. Detailed seismic velocity of the incoming subducting sediments in the 2004 great Sumatra earthquake rupture zone from full waveform inversion of long offset seismic data. *Geophysical Research Letters* **44**, 3090–3099 (2017).

54. Hardebeck, J. L. & Loveless, J. P. Creeping subduction zones are weaker than locked subduction zones. *Nature Geoscience* **11**, 60–64 (2018).

55. Yang, H., Yao, S., He, B. & Newman, A. V. Earthquake rupture dependence on hypocentral location along the Nicoya Peninsula subduction megathrust. *Earth and Planetary Science Letters* **520**, 10–17 (2019).

56. Singh, S. C. *et al.* Aseismic zone and earthquake segmentation associated with a deep subducted seamount in Sumatra. *Nature Geoscience* **4**, 308–311 (2011).

57. Aochi, H. & Ide, S. Conceptual multi-scale dynamic rupture model for the 2011 off the Pacific coast of Tohoku Earthquake. *Earth, Planets and Space* **63**, 761–765 (2011).

58. Ide, S. & Aochi, H. Historical seismicity and dynamic rupture process of the 2011 Tohoku-Oki earthquake. *Tectonophysics* **600**, 1–13 (2013).

59. Seno, T. Determination of the pore fluid pressure ratio at seismogenic megathrusts in subduction zones: Implications for strength of asperities and Andean-type mountain building. *Journal of Geophysical Research* **114**, B05405 (2009).

60. Seno, T. Subducted sediment thickness and M_W 9 earthquakes. *Journal of Geophysical Research: Solid Earth* **122**, 470–491 (2017).

61. Heuret, A., Conrad, C. P., Funiciello, F., Lallemand, S. & Sandri, L. Relation between subduction megathrust earthquakes, trench sediment thickness and upper plate strain. *Geophysical Research Letters* **39** (2012).

62. Scholl, D. W. *et al.* Great (Mw8.0) megathrust earthquakes and the subduction of excess sediment and bathymetrically smooth seafloor. *Geosphere* **11**, 236–265 (2015).

63. Curray, J. R. Sediment volume and mass beneath the Bay of Bengal. *Earth and Planetary Science Letters* **125**, 371–383 (1994).

64. Subarya, C. *et al.* Plate-boundary deformation associated with the great Sumatra–Andaman earthquake. *Nature* **440**, 46 (2006).

65. Nishikawa, T. *et al.* The slow earthquake spectrum in the Japan Trench illuminated by the S-net seafloor observatories. *Science* **365**, 808–813 (2019).

66. Oeser, J., Bunge, H.-P. & Mohr, M. Cluster design in the Earth sciences: Tethys. In *International conference on high performance computing and communications*, 31–40 (Springer, 2006).

67. LeVeque, R. J., George, D. L. & Berger, M. J. Tsunami modelling with adaptively refined finite volume methods. *Acta Numerica* **20**, 211–289 (2011).

68. Berger, M. J., George, D. L., LeVeque, R. J. & Mandli, K. T. The GeoClaw software for depth-averaged flows with adaptive refinement. *Advances in Water Resources* **34**, 1195–1206 (2011).

69. Laske, G., Masters, G., Ma, Z. & Pasyanos, M. Update on CRUST1.0 — a 1-degree global model of Earth's crust. In *Geophys. Res. Abstr*, vol. 15, 2658 (EGU General Assembly Vienna, Austria, 2013).

70. Weatherall, P. *et al.* A new digital bathymetric model of the world's oceans. *Earth and Space Science* **2**, 331–345 (2015).

71. Wirp, S. A. *et al.* 3D linked subduction, dynamic rupture, tsunami and inundation modeling: dynamic effects of supershear and tsunami earthquakes, hypocenter location and shallow fault slip. *Frontiers in Earth Science* **9**, 177 (2021).

72. Dziewonski, A. M. & Anderson, D. L. Preliminary reference Earth model. *Physics of the earth and planetary interiors* **25**, 297–356 (1981).

73. Hayes, G. P. *et al.* Slab2, a comprehensive subduction zone geometry model. *Science* **362**, 58–61 (2018).

74. Banerjee, P., Pollitz, F., Nagarajan, B. & Burgmann, R. Coseismic Slip Distributions of the 26 December 2004 Sumatra-Andaman and 28 March 2005 Nias Earthquakes from GPS Static Offsets. *Bulletin of the Seismological Society of America* **97**, S86–S102 (2007).

75. Lin, J.-Y., Pichon, X. L., Rangin, C., Sibuet, J.-C. & Maury, T. Spatial aftershock distribution of the 26 December 2004 great Sumatra-Andaman earthquake in the northern Sumatra area. *Geochemistry, Geophysics, Geosystems* **10** (2009).

76. Hardebeck, J. L. Coseismic and postseismic stress rotations due to great subduction zone earthquakes. *Geophysical Research Letters* **39** (2012).

77. Aochi, H. & Madariaga, R. The 1999 Izmit, Turkey, earthquake: Nonplanar fault structure, dynamic rupture process, and strong ground motion. *Bulletin of the Seismological Society of America* **93**, 1249–1266 (2003).

78. Gahalaut, V. K. & Gahalaut, K. Burma plate motion. *Journal of Geophysical Research* **112**, B10402 (2007).

79. Hardebeck, J. L. & Hauksson, E. Crustal stress field in southern California and its implications for fault mechanics. *Journal of Geophysical Research: Solid Earth* **106**, 21859–21882 (2001).

80. Byerlee, J. Friction of rocks. *Pure and Applied Geophysics* **116**, 615–626 (1978).

81. Melgar, D. & Hayes, G. P. Systematic Observations of the Slip Pulse Properties of Large Earthquake Ruptures. *Geophysical Research Letters* **44**, 9691–9698 (2017).

82. Ma, S. A self-consistent mechanism for slow dynamic deformation and tsunami generation for earthquakes in the shallow subduction zone. *Geophysical Research Letters* **39** (2012).

83. Dumbser, M. & Käser, M. An arbitrary high-order discontinuous Galerkin method for elastic waves on unstructured meshes – II. the three-dimensional isotropic case. *Geophysical Journal International* **167**, 319–336 (2006).

84. Pelties, C., de la Puente, J., Ampuero, J.-P., Brietzke, G. B. & Käser, M. Three-dimensional dynamic rupture simulation with a high-order discontinuous Galerkin method on unstructured tetrahedral meshes. *Journal of Geophysical Research: Solid Earth* **117** (2012).

85. Uphoff, C. *et al.* Extreme scale multi-physics simulations of the tsunamigenic 2004 sumatra megathrust earthquake. In *Proceedings of the International Conference for High Performance Computing, Networking, Storage and Analysis, SC 2017* (2017).

86. Breuer, A. *et al.* Sustained Petascale Performance of Seismic Simulations with SeisSol on SuperMUC. In *Supercomputing. ISC 2014. Lecture Notes in Computer Science, vol 8488*, 1–18 (Springer, Cham, 2014).

87. Heinecke, A. *et al.* Petascale High Order Dynamic Rupture Earthquake Simulations on Heterogeneous Supercomputers. In *SC14: International Conference for High Performance Computing, Networking, Storage and Analysis*, 3–14 (IEEE, New Orleans, LA, USA, 2014).

88. Rettenberger, S., Meister, O., Bader, M. & Gabriel, A.-A. Asagi: A parallel server for adaptive geoinformation. In *Proceedings of the Exascale Applications and Software Conference 2016*, EASC '16, 2:1–2:9 (ACM, New York, NY, USA, 2016).

89. Wollherr, S., Gabriel, A.-A. & Uphoff, C. Off-fault plasticity in three-dimensional dynamic rupture simulations using a modal Discontinuous Galerkin method on unstructured meshes: implementation, verification and application. *Geophysical Journal International* **214**, 1556–1584 (2018).

90. Pelties, C., Gabriel, A.-A. & Ampuero, J.-P. Verification of an ADER-DG method for complex dynamic rupture problems. *Geoscientific Model Development* **7**, 847–866 (2014).

91. Harris, R. A. *et al.* Verifying a computational method for predicting extreme ground motion. *Seismological Research Letters* **82**, 638–644 (2011).

92. Harris, R. A. *et al.* A Suite of Exercises for Verifying Dynamic Earthquake Rupture Codes. *Seismological Research Letters* **89**, 1146–1162 (2018).

93. Madden, E. H. *et al.* Linked 3-D modelling of megathrust earthquake-tsunami events: from subduction to tsunami run up. *Geophysical Journal International* **224**, 487–516 (2021).

94. Tanioka, Y. & Satake, K. Tsunami generation by horizontal displacement of ocean bottom. *Geophysical Research Letters* **23**, 861–864 (1996).

95. Abrahams, L., Dunham, E., Krenz, L., Saito, T. & Gabriel, A.-A. Comparison of techniques for coupled earthquake and tsunami modeling. other, Geophysics (2021). URL `http://www.essoar.org/doi/10.1002/essoar.10506178.2`.

96. Hanson, J. A. & Bowman, J. R. Dispersive and reflected tsunami signals from the 2004 Indian Ocean tsunami observed on hydrophones and seismic stations. *Geophysical Research Letters* **32** (2005).

97. Kim, J., Pedersen, G. K., Løvholt, F. & LeVeque, R. J. A Boussinesq type extension of the GeoClaw model - a study of wave breaking phenomena applying dispersive long wave models. *Coastal Engineering* **122**, 75–86 (2017).

98. Saito, T., Baba, T., Inazu, D., Takemura, S. & Fukuyama, E. Synthesizing sea surface height change including seismic waves and tsunami using a dynamic rupture scenario of anticipated Nankai trough earthquakes. *Tectonophysics* 228166 (2019).

99. Tsai, V. C., Ampuero, J.-P., Kanamori, H. & Stevenson, D. J. Estimating the effect of Earth elasticity and variable water density on tsunami speeds. *Geophysical Research Letters* **40**, 492–496 (2013).

100. Lotto, G. C., Jeppson, T. N. & Dunham, E. M. Fully Coupled Simulations of Megathrust Earthquakes and Tsunamis in the Japan Trench, Nankai Trough, and Cascadia Subduction Zone. *Pure and Applied Geophysics* **176**, 4009–4041 (2019).

101. Krenz, L. *et al.* T52C-09: Elastic-Acoustic Coupling for 3D Tsunamigenic Earthquake Simulations with ADER-DG on Unstructured Tetrahedral Meshes. In *AGU Fall Meeting 2019* (San Francisco, 2019). URL `https://ui.adsabs.harvard.edu/abs/2019AGUFM.T52C..09K/abstract`.

102. Krischer, L. *et al.* On-demand custom broadband synthetic seismograms. *Seismological Research Letters* **88**, 1127–1140 (2017).

103. Wyllie, D. C. & Mah, C. *Rock slope engineering* (CRC Press, 2004).

104. Roten, D., Olsen, K. B. & Day, S. M. Off-fault deformations and shallow slip deficit from dynamic rupture simulations with fault zone plasticity. *Geophysical Research Letters* **44**, 7733–7742 (2017).

105. Gabriel, A.-A., Ampuero, J.-P., Dalguer, L. A. & Mai, P. M. Source properties of dynamic rupture pulses with off-fault plasticity. *Journal of Geophysical Research: Solid Earth* **118**, 4117–4126 (2013).

106. Ma, S. A physical model for widespread near-surface and fault zone damage induced by earthquakes. *Geochemistry, Geophysics, Geosystems* **9** (2008).

107. Krüger, F. & Ohrnberger, M. Tracking the rupture of the M w = 9.3 Sumatra earthquake over 1,150 km at teleseismic distance. *Nature* **435**, 937 (2005).

108. McCaffrey, R. The tectonic framework of the Sumatran subduction zone. *Annual Review of Earth and Planetary Sciences* **37**, 345–366 (2009).

109. Yoshimoto, M. & Yamanaka, Y. Teleseismic inversion of the 2004 Sumatra-Andaman earthquake rupture process using complete Green's functions. *Earth, Planets and Space* **66** (2014).

110. Okuda, T. & Ide, S. Hierarchical rupture growth evidenced by the initial seismic waveforms. *Nature Communications* **9**, 3714 (2018).

111. Gupta, S., Borah, K. & Saha, G. Continental like crust beneath the Andaman Island through joint inversion of receiver function and surface wave from ambient seismic noise. *Tectonophysics* **687**, 129–138 (2016).

112. Bletery, Q., Sladen, A., Jiang, J. & Simons, M. A Bayesian source model for the 2004 great Sumatra-Andaman earthquake. *Journal of Geophysical Research: Solid Earth* **121**, 5116–5135 (2016).

113. Day, S. M., Dalguer, L. A., Lapusta, N. & Liu, Y. Comparison of finite difference and boundary integral solutions to three-dimensional spontaneous rupture. *Journal of Geophysical Research* **110**, B12307 (2005).

ACKNOWLEDGMENTS

We thank Leonhard Rannabauer, Stefan Vater, and Jihwan Kim for their support in setting up tsunami simulations. We thank Stephanie Wollherr, Carsten Uphoff, Michael Bader, Sebastian Rettenberger, Casper Pranger, Thorne Lay, and Jörn Behrens for fruitful discussion. We thank Mohamed Chlieh for providing his kinematic model of the Sumatra-Andaman event. We thank Associate Editor Stefan Lachowycz, two anonymous reviewers and Eric Dunham for their constructive suggestions.

Funding

The authors acknowledge funding from the Volkswagen Foundation (project “ASCETE”, grant no. 88479), the European Union’s Horizon 2020 research and innovation programme (ChEESE project, grant agreement No. 823844; TEAR ERC Starting grant no. 852992), the German Research Foundation (DFG) (projects KA 2281/4-1, GA 2465/2-1, GA 2465/3-1), by KAUST-CRG (GAST, grant no. ORS-2016-CRG5-3027 and FRAGEN, grant no. ORS-2017-CRG6 3389.02), by KONWIHR – the Bavarian Competence Network for Technical and Scientific High Performance Computing (project NewWave), and by BayLat – the Bavarian University Centre for Latin America. Computing resources were provided by the Institute of Geophysics of LMU Munich (*66*) and the Leibniz Supercomputing Centre (LRZ, projects no. h019z, pr63qo, and pr45fi).

Author contributions

Modeling was conducted by T.U. under the supervision of A.-A. G.. A.-A. G. initiated the project. E.H.M. designed the splay faults model. The manuscript was written jointly by T.U., A.-A. G. and E.H.M..

Competing interests

The authors declare no competing interests and no conflict of interests.

Data and materials availability

The authors declare that all data supporting the findings of this study are available within the paper and its Methods section. In particular, all data required to reproduce the earthquake scenario can be downloaded from `https://syncandshare.lrz.de/getlink/fiVhiJYfKcb5a2PzkuNMNyxu/`. We use the following projection: WGS 84 / UTM Mercator 46N (EPSG:32646). We use SeisSol, commit 7108d554e994c6c052d77910de09bf41a1500bee, available on Github. The procedure to download, compile, and run SeisSol is described in its documentation (`https://seissol.readthedocs.io`). All data required to reproduce the tsunami scenarios can be downloaded from `https://syncandshare.lrz.de/getlink/fiFzhTedQ1dchnFHrc2T98W9/`. We use the GeoClaw (*67, 68*), v5.8.0, available on GitHub. Sea surface height anomalies derived from the Jason-1 data record are available at `ftp://podaac-ftp.jpl.nasa.gov/allData/jason1/L2/j1_ssha/c109/`.

LIST OF SUPPLEMENTARY MATERIALS

Methods and Supplementary Information

Supplementary Text

Figs. E1 to E9 and S1

Table E1 and S1

References (68-113)

METHODS

Regional lithological structure

We construct a 3D subsurface computational model of the Sumatra-Andaman region to capture spatial variations of lithology and seismic rock properties. The model incorporates a complex subduction interface, large-scale layers varying in thickness (*69*), and topography and bathymetry data (*70*) (see Supplementary information Sect. “3D velocity model”). We add a 3 km wide layer to the velocity structure enclosing the subduction interface. Within this approximated subduction channel, strong along-depth rigidity variations are incorporated (Fig. 1e), that we constrain from recent global V_p velocity models (*5*) in agreement with earlier global inferences from earthquake rupture duration (*1, 9*) We increase rigidity piecewise linearly with depth (*5*) from 5 to 43 MPa, thus accounting for softer rocks at shallow depth, including materials scraped off the oceanic crust and younger deposits (Fig. 1e). (*5*) empirically derive density and shear wave velocity from V_p which includes the assumption that Poisson ratio increases from 0.25 to 0.35 towards shallower depths. Dynamic rupture modeling increasing Poisson ratio has been associated with enhanced shallow fault slip and tsunami potential (*71*). Also, (*5*)’s global average is defined with respect to an absolute interplate boundary depth. In our subduction channel velocity model we approximate the seafloor depth with respect to the water surface as ranging from 5 km in the south to 3 km in the northern model region accounting for along-arc variation (*70*).

We demonstrate the importance of the assumed 3D velocity structure including the strong rigidity variations in the subduction channel in Methods Sect. "The importance of strongly depth-dependent rigidity") by comparison to a 1D PREM (Preliminary Reference Earth Model, (*72*)) velocity structure scenario .

Fault geometry

We construct a non-planar model of the subduction interface and possible splay faults that may have ruptured during the 2004 earthquake (Figs.1c and 2a). The slab interface is based on the geometry of Slab 2.0 (*73*). Evidence that splay faults slipped coseismically during the 2004 event stems from large tsunami run-ups observed in Aceh province in the near-source region (e.g., (*74*)), high reflectivity in shallow seismic reflection data (*31*), and aftershocks (*33, 75*), the double peak in the tsunami waves recorded by the Jason-1 satellite (*32*), alongside other observations (e.g., (*29*)). We add one long forethrust dipping 65° landward and two backthrust faults dipping 65° trenchward. Each extends from their inferred trace to the megathrust interface. The forethrust unifies the Upper Splay Fault mapped by (*29*) and the splay fault suggested by (*32*). The northern backthrust is mapped from seismic reflection data by (*29*) and (*30*) and the southern backthrust is identified by (*31*) from seismic reflection data. The true extent of these faults are not known; mapped lengths are restricted to the area of data coverage.

Stress state and fault friction

The stresses acting on faults and their strength, which are key initial conditions of dynamic rupture models, are poorly known. Laboratory experiments offer insight on frictional strength parameters, but extrapolating these results to a natural scale is complicated. We introduce new procedures to constrain these parameters from stress inversion results (*76*), including the inference of coseismic rotation of the principal stress axes (*4, 76*).

Principal stress orientations and magnitudes

In line with (*76*)'s results, we apply a non-Andersonian initial stress field that features a shallowly plunging maximum compressive stress axis (σ_1), a near-horizontal intermediate stress axis (σ_2), and a steeply plunging minimum principal stress (σ_3). σ_1 plunges at 22 °, which optimally stresses a fault dipping 8°.

We align stress inversion and geodetic observations in choosing the σ_1 orientation. The model accounts for the inferred clockwise rotation of σ_1 from 309° in the South to 330° in the North (*76*), with a linear transition over 2° near 5° latitude (see Fig. 1a). This leads to synthetic displacements with orientations in overall agreement with geodetic observations.

The principal stress magnitudes are systematically constrained based on seismo-tectonic observations, fault fluid pressurization, and the Mohr-Coulomb theory of frictional failure.

Rupture dynamics are in their general sense governed by the stress drop and the fault strength. These are constrained by the effective confining stress, the fault friction drop $\mu_\mathrm{s} - \mu_\mathrm{d}$ (where μ_s and μ_d are the static and dynamic friction coefficients, respectively) and the relative prestress ratio R_0. The latter is defined as the ratio of prestress over strength drop (e.g., (*77*)):

$$R = (\tau_0 - \mu_\mathrm{d}\sigma_\mathrm{n})/((\mu_\mathrm{s} - \mu_\mathrm{d})\sigma_\mathrm{n}) \,, \tag{1}$$

where τ_0 and σ_n are the initial shear and normal tractions on a fault plane. R_0 is the maximum value of R, associated with a virtual, optimally-oriented fault plane.

We assume lithostatic pressure,

$$\sigma_\mathrm{c}(z) = \int_0^z \rho(z_i) g z_i dz_i, \tag{2}$$

and a near-lithostatic fluid pressure, $P_\mathrm{f} = 0.974\sigma_\mathrm{c}$, to ensure a realistic stress drop. The resulting effective confining stress increases with depth with a gradient of ≈1 MPa/km. From 25–45 km depth, we taper the deviatoric stresses to zero to represent the transition from a brittle to a ductile regime.

We account for along-arc variations in convergence rate by varying the initial stress along-strike of the megathrust. Observations by (*76*) suggest that the strain accumulated since the last great earthquake, inferred using along-arc variations in convergence rate, is consistent with the along-arc variation in slip inferred for the 2004 earthquake, which is characterized by more slip in the south than in the north.

We modulate R_0 by the convergence rate inferred from rigid plate tectonics considerations, using the Euler pole inferred by (*78*) (see Fig. 1b). This modulation is applied over the full rupture length.

We demonstrate the importance of along-arc prestress modulation in Methods Sect. "The importance of convergence-rate modulated regional driving stresses") by comparing to a scenario in which no prestress modulations are considered.

Coseismic stress rotation to constrain fault friction

The inference of coseismic rotation of the principal stress axes (see Fig. 1c) during the 2004 earthquake (*4, 76*) constrains the ratio of the stress drop over the prestress. A significant principal stress rotation indicates that the stress drop is large enough to change the deviatoric background stress (e.g., (*79*)), that is the prestress and the stress drop are of the same order. This can lead to a sudden switch of orientation of principal axes of stress, as suggested by the occurrence of normal faulting following megathrust earthquakes (*4, 76*) .

We estimate the average stress drop $d\tau$ in the dynamic rupture model as

$$d\tau \sim (\mu_\mathrm{s} - \mu_\mathrm{d}) R_0 (\sigma_\mathrm{c} - P_\mathrm{f}). \tag{3}$$

We define ξ as the ratio of residual shear traction over prestress to get

$$\xi \sim \frac{\mu_\mathrm{d}}{(\mu_\mathrm{s} - \mu_\mathrm{d}) R_0 + \mu_\mathrm{d}}, \tag{4}$$

which can be written as

$$\mu_\mathrm{d} \sim \frac{\mu_\mathrm{s}}{(1-\xi)/(R_0 \xi) + 1}. \tag{5}$$

Eq. 5 relates μ_d to μ_s and R_0. Assuming a static friction value of $\mu_\mathrm{s} = 0.6$ (*80*), a ratio of residual shear traction over prestress of $\xi = 0.4$, as inferred in the southern part of the rupture (*76*)), and a ratio of prestress over strength drop of $R_0 = 0.65$, yields $\mu_\mathrm{d} = 0.18$. Based on these considerations, we use a linear slip weakening friction law setting $\mu_\mathrm{s} = 0.6$, $\mu_\mathrm{d} = 0.2$ and $D_\mathrm{c} =$ 2.5 m. The relatively large D_c allows recovering the northern rupture arrest, as well as an average rupture speed comparable with published inferences (see Fig 2d). It leads to a wide process zone in our model, which may reflect the larger slip pulse width associated with large megathrust earthquakes (e.g., (*81*)). At shallow depth above 10 km we linearly increase μ_d. Fault friction is then slip neutral at 5 km depth and slip strengthening above. In the Southern rupture region, transition to slip strengthening occurs 5 km deeper.

Earthquake computational model

Computational earthquake models that are able to account for the curved thrust interface and splay fault networks intersecting with bathymetry, the narrow accretionary wedge, and the complex lithology of subduction zones are challenging. Off-fault yielding processes, which can significantly modulate fault slip near the trench (e.g., (*45, 82*)), pose additional computational demands. These challenges are addressed using the SeisSol software package (e.g., (*83–85*)), which solves the nonlinear coupled problem of spontaneous frictional failure across prescribed fault surfaces, seismic wave propagation, and (visco-)plastic Drucker-Prager off-fault damage (*42*).

SeisSol is based on an Arbitrary high-order accurate DERivative Discontinuous Galerkin method (ADER-DG, (*83*)) and solves the seismic wave equations with high-order accuracy in space and time. SeisSol uses fully non-uniform, adaptive, unstructured tetrahedral meshes enabling geometrically complex models, including curved and mutually intersecting faults. Mesh resolution can be adapted to ensure fine sampling of the faults while satisfying the requirements regarding numerical dispersion of pure wave propagation away from the fault. End-to-end computational optimization (*86–89*), including an efficient local time-stepping algorithm (*85*), allows for high efficiency on high-performance computing infrastructure. SeisSol is verified in a wide range of community benchmarks (*90*) by the SCEC/USGS Dynamic Rupture Code Verification project (*91, 92*). SeisSol is freely available (`https://github.com/SeisSol/SeisSol`).

Tsunami modeling

To model the tsunami, we use GeoClaw (*67, 68*), a highly scalable software solving the shallow water equations using adaptive mesh refinement. GeoClaw implements a shock-capturing finite volume method on logically rectangular latitude–longitude grids on the sphere. Its adaptive mesh refinement approach allows for stable and accurate simulation of large-scale wave propagation in the deep sea and small-scale wave shoaling and inundation at the shore.

We use the GEBCO 2019 topography and bathymetry data set (*70*) with a horizontal resolution of 15 arc seconds (approximately 450 m). This allows for a sufficiently accurate representation of bathymetric features in deeper sea regions, where tsunamis have large wavelengths, but is relatively inaccurate at shallow depths.

The tsunami is sourced by time-dependent bathymetry perturbations resembling the coseismic dynamic rupture seafloor displacements (*93*). In addition to the vertical displacement, we account for the effects of east-west and north-south horizontal displacements by the linear approximation proposed by (*94*).

The domain of the computational tsunami model (Fig. 4c) encompasses the source region and a large part of the Indian ocean. The computational grid incorporates 2 levels of dynamically adaptive mesh refinement, with a respective resolution of 45 and 90 arc seconds (≈1300 m and 2600 m). The simulation is run for 2 h 30 min (simulation time).

Our hydrostatic shallow-water based tsunami modeling approach may be extended to capture also smaller-scale complexity during tsunami-genesis (e.g. (*95*)) and dispersive effects during tsunami wave propagation (e.g. (*96*)), by allowing for a non-linear hydrodynamic response (e.g. (*97, 98*)), corrections for dispersive Earth elasticity and non-dispersive water compressibility (*99*), or fully coupled seismic, acoustic and gravity modeling (*100, 101*).

Teleseismic model validation

Following (*43*), we translate the time histories of dynamic fault slip of the dynamic rupture scenario into a subset of 50 double couple point sources (25 along strike by 2 along depth). To that purpose, we subdivide the fault in 50 subregions. We compute the moment rate as $G\frac{dS}{dt}$ where S is the slip and G the local rigidity in the dynamic rupture model at the center of each fault element face. The equivalent moment tensor of each fault element face is calculated from the rake of the accumulated slip and each fault face orientation in terms of strike and dip angle. The moment tensor of each subregion is computed by summing the moment tensors of each fault element face within a subregion. The respective location of the equivalent moment tensor is calculated as the mean of the locations of the barycenters of each slipping fault element face weighted by its moment magnitude. We generate broadband synthetics from a Green's function database using Instaseis (*102*), which is based on global 2.5D axisymmetric spectral element simulations, and the PREM model (Preliminary Reference Earth Model, (*72*)) for a maximum period of 10 s and including anisotropic effects.

The in this manner rapidly computed, yet simplified, teleseismic synthetics reproduce the recorded long-period teleseismic waveforms with an average rRMS of 0.7 for the preferred dynamic rupture scenario at periods of 150 s to 500 s (Fig. E3). The arrival times and amplitudes of the surface waves at the frequency considered (150 s to 500 s) is well recovered at most stations. The envelopes of the recorded long-period teleseismic waveforms are also overall well captured, with noticeable discrepancies in rupture forward direction (HYB, LSA and ENH).

The teleseismic waveform synthetics combine InstaSeis' Green's functions based on a PREM model with dynamic rupture equivalent moment tensor point sources, and thus do not account for the off-fault 3D velocity structure we use in the dynamic model. Accounting accurately for the seismic potency contribution of the low-rigidity shallow parts of the megathrust would require fully coupled dynamic rupture and seismic wave propagation simulations across teleseismic distances. However, this is currently computationally not feasible in the scope of thorough sensitivity analysis.

Off-fault plasticity

We account for the possibility of off-fault inelastic energy dissipation by adopting a Drucker-Prager elasto-viscoplastic rheology. The implementation is described in (*89*). While purely elastic dynamic rupture models require defining initial stresses acting on the fault(s) only, models with off-fault plasticity require domain-wide parametrization of initial stresses, cohesion, and friction of the bulk rock.

Off-fault initial stresses resemble the depth-dependent initial stresses described in Methods Sec. "Stress state and fault friction". The viscoplastic relaxation time T_v is set to 0.03 s.

Cohesion and bulk friction are challenging to constrain. For example, the strength of drill core samples which are often free of pre-existing cracks may not be representative of the fractured rock mass in a fault zone (*103*). High-resolution geophysical imaging is required to resolve the geometrical complexities and characterize the damage state of megathrust fault zones (*11*). In line with our focus on regional driving factors, we here use a simple cohesion model averaging local effects with a limited number of parameters. We assume that effective off-fault deformation shall be limited to shallow depths (< 15-20 km) by adapting a linear dependence of bulk cohesion on the effective confining pressure (*104*). We introduce an additional constant term to allow for modulation of the severity of plastic deformation at shallow depths in between scenarios. Then, the bulk cohesion $C(z)$ is set as (see Fig. E4a):

$$C(z) = C_0 + C_1(z)\sigma'_\text{c}. \tag{6}$$

$C_1(z)$ accounts for the hardening of the rock structure with depth, while C_0 controls localization and magnitude of off-fault yielding at shallow depth and $\sigma'_\text{c} = \sigma_\text{c} - P_\text{f}$ is the effective confining stress.

We set C_0 to 1 MPa in the base dynamic rupture scenario to represent partially consolidated sediments (*35*), to 0.3 MPa for the alternative scenario featuring weaker sediments, and to 10 MPa for the alternative model featuring stronger sediments. $C_1(z) = 1$ for both the base model and the alternative model featuring stronger sediments, and $C_1(z) = \max(1, (z/18000)^2)$ for the alternative model featuring weaker sediments.

To enhance the shallow effectiveness of off-fault plasticity without causing wide-spread yielding at depths deeper than 15–20 km we decrease the internal frictional shear strength of the bulk rock in the weak sediment model. The bulk material's internal friction coefficient ν is set equal to the static fault friction coefficient, $\mu_\text{s} = 0.6$. In the weaker sediments scenario only, we linearly decrease it at shallow depth, from 0.6 at 18 km to 0.2 at the sea-surface. Exploring additional hypotheses or observationally driven cohesion models is left to future work. For instance, (*104*) propose a procedure based on the Geological Strength Index (GSI) and the Hoek-Brown model that may be adapted to constrain a locally heterogeneous cohesion model.

Closeness to failure (see Fig. E4a) is quantified by the CF ratio (e.g., (*82*)):

$$CF = \frac{\sqrt{I_2}}{\tau_\mathrm{c}} \tag{7}$$

where I_2 is the second invariant of the deviatoric stresses and τ_c the Drucker-Prager yield criterion, given by:

$$\tau_\mathrm{c} = C(z)\cos(\Phi) - \sigma_\mathrm{m}\sin(\Phi) \tag{8}$$

with $\Phi = \arctan(\nu)$ the internal angle of friction and $\sigma_\mathrm{m} = \sum_{n=1}^{3} \sigma_{ii}/3$ the mean stress.

The such constrained CF ratio is depth-dependent and varies along-arc for all three scenarios presented, aligned with the assumed distribution of initial stresses. In the base and stronger sediment scenarios, cohesion is dominated by the constant term C_0 at shallow depth. Closeness to failure is there low, while plastic yielding is not prevented since absolute rock strength is low as well. In the weak sediment model, a quadratic reduction of cohesion $C(z)$ down to a depth of 18 km leads to pronounced higher closeness to failure peaking at 4 km depth. At larger depth, CF decreases according to the same linear increase of bulk cohesion with depth in all models. We note that even in the weak sediment model, deeper wedge rocks are not on the verge of failure as is assumed in e.g. (*45*).

The total seismic moment $M_{0,\mathrm{t}}$ is the sum of the moment due to slip on the fault, $M_{0,\mathrm{e}}$, and the moment due to off-fault plastic strain, $M_{0,\mathrm{p}}$. We adapt previous 2D inferences (e.g., (*105*)) to our 3D non-associated Drucker–Prager plasticity implementation (*89*) and compute:

$$M_{0,\mathrm{p}} = \sum_{i=1}^{N} \mu V \eta, \tag{9}$$

with μ being the rigidity, V the volume of each tetrahedral element i and η a scalar quantity measuring the accumulated material damage at the end of the dynamic rupture simulation. Following (*106*) it is

$$\eta(t) = \int_0^t d\eta = \int_0^t \sqrt{\frac{1}{2}\dot{\epsilon}_{ij}^{p}\dot{\epsilon}_{ij}^{p}}, \tag{10}$$

with $\dot{\epsilon}_{ij}^{p}$ being the inelastic strain rate. The contribution of plastic strain to the total moment is small for the base and stronger sediments scenarios but non-negligible ($M_{0,\mathrm{p}}\,/M_{0,\mathrm{t}} \approx 7.5\%$) in the weaker sediment scenario (Table E1).

Ratios of $M_{0,\mathrm{p}}/M_{0,\mathrm{e}}$ which are on the order of a few percent are consistent with 2D pulse-like dynamic rupture simulations (*105*) at comparable relative fault strength S, with $S = (1 - R)/R$. However, the contribution of plastic moment can become dominant under certain conditions, such as large S and large angles between the maximum compressive stress and the fault. This may be explored in future work focusing specifically on relatively slow tsunami earthquakes (*52*).

Off-fault plastic deformation affects all here presented scenarios compared to a purely elastic model (Fig.E5a). Specifically, earthquake rupture dynamics of a fully elastic scenario, with no off-fault yielding, differ from the stronger sediment scenario as illustrated in Fig.E5a: specifically near the trench, fully elastic fault slip is considerably increased to a maximum of 52 m. Fully elastically sourced tsunami synthetics (Fig.E5b) are overall similar to the base and stronger sediment scenarios and also reproduce the early two tsunami peaks.

The importance of strongly depth-dependent rigidity

We demonstrate the importance of strongly depth-dependent rigidity in an alternative model, which adopts a 1D PREM (*72*) velocity structure. To generate a comparable dynamic rupture earthquake scenario requires few changes to the model. We increase the nucleation radius from 10 to 15 km and the maximum normalized prestress ratio R_0 from 0.65 to 0.75 to restore the rupture potential of the megathrust. The PREM alternative earthquake scenario yields a comparable slip distribution to the base model (Fig. E6a), and therefore fits GPS observations well (Fig E6d,e). However, its moment magnitude $M_\mathrm{w} = 9.32$ is higher than most kinematic models (based on body and surface waves, normal models, GPS, corral uplift or Rayleigh waves (*26*)). Rupture speed of the PREM model is faster which is shortening rupture duration to 450s. This is 50s to 100s shorter than most inferences from normal, body and surface wave inversion as well as back-projection (e.g. (*17, 21, 25, 107*)). In distinction to the along-depth variation of rupture speed and the boomerang-shaped slip pulse of the base scenario, rupture speed and slip rates in the PREM scenario (Fig. E6b and supplementary animation Sumatra_SR_base_PREM.mp4) are rather homogeneous along-depth and along-margin. Also, the PREM slip pulse is smoother and wider. The moment release rate exceeds teleseismic inversions by almost a factor of 2 during the first 150 s of rupture time (Fig. E6c). While assuming weaker sediments may recover a more realistic earthquake duration (Fig.E8c), this would not change the scenario's moment magnitude. The PREM scenario, as well as alternatives that we performed that lack strongly depth-dependent rigidity, highlights the importance of this complexity in producing realistic scenarios.

The importance of convergence-rate modulated regional driving stresses

To demonstrate the importance of along-arc variations in prestress modulated by convergence rate, we detail an alternative dynamic rupture earthquake scenario in which no regional prestress variations are considered (Fig. E7). This scenario has considerably more fault slip in the North, at latitudes above 8 °. We infer that the interplay of regional-scale tectonic variations, fault loading and frictional strength govern megathrust dynamics and that these factors cannot be treated in isolation. To account for this complexity is permitted by the multi-physics modeling approach taken here.

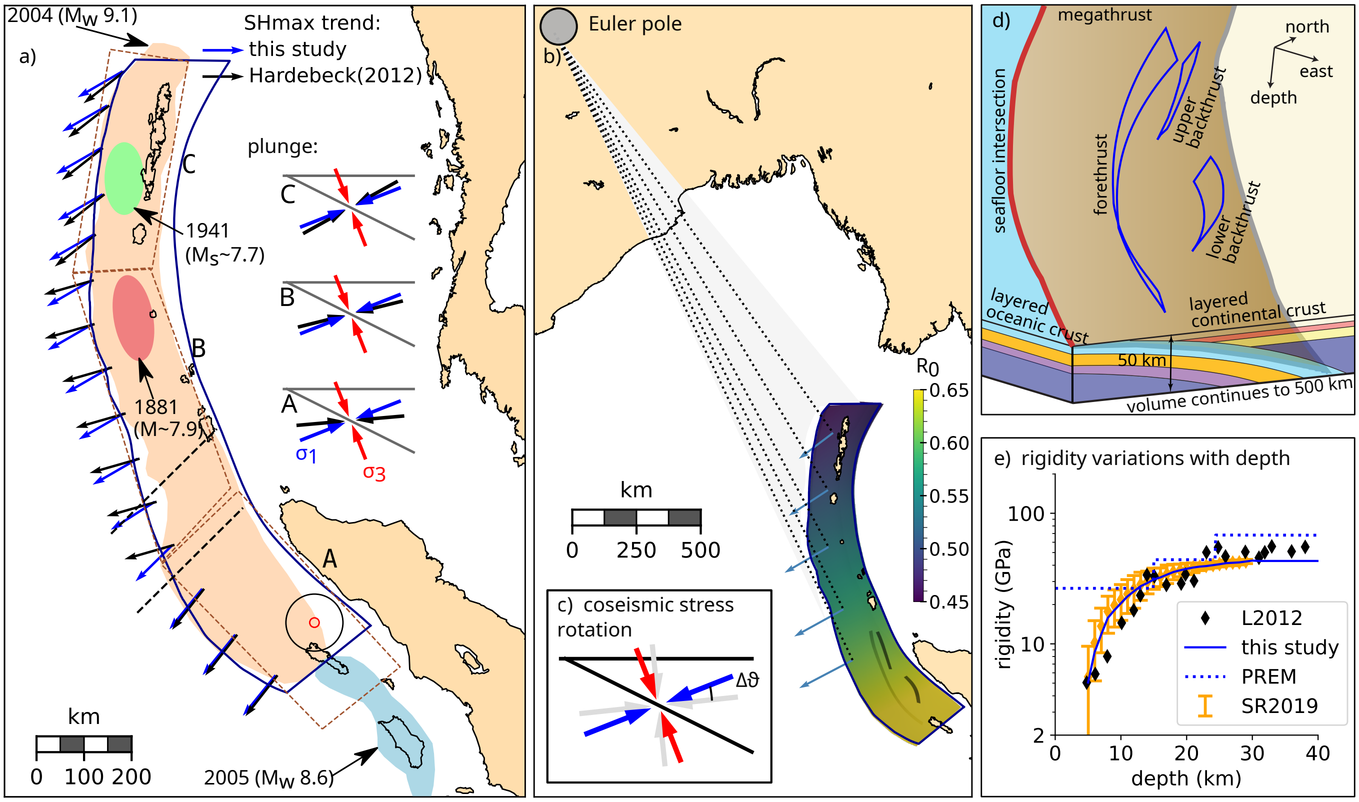

Figure 1: Key subduction characteristics constraining a 3D dynamic rupture model of a megathrust earthquake. (a) Tectonic setting and stress state of the Sumatra-Andaman subduction zone. Dark blue lines delineate the projected fault interface. Coloured shapes are slip areas for the 2004 and three historic megathrust earthquakes adapted from (*108*). Dashed brown polygons indicate locations of regions A, B and C over which stress parameters are inverted by (*76*). Arrows compare the trends of the maximum horizontal stress (SH$_{\text{max}}$) used in this scenario (blue) to those by (*76*) (black). Dashed black lines bound the region where the trend of $\sigma_\mathbf{1}$ linearly increases from 309° to the south to 330° to the north in this scenario. Cross-sections show the plunge of $\sigma_\mathbf{1}$ (blue) and the minimum principal stress ($\sigma_\mathbf{3}$, red) used in this scenario, compared to those in (*76*) (black). Red (radius 10 km) and black (radius 60 km) circles, centered at the hypocenter, bound the region where the slip weakening distance (D_c) increases linearly from 1.0 to 2.5 m. (b) Modulation of the relative prestress ratio R_0 by the magnitude of the convergence rate inferred from rigid plate tectonics considerations, using the Euler pole inferred by (*78*) (grey dot). (c) Rotation of the maximum, $\sigma_\mathbf{1}$ (grey to blue), and minimum, $\sigma_\mathbf{3}$ (grey to red) principal stress axes due to an earthquake (adapted from (*76*)). (d) Schematic view of the here adapted regional 3D structural model (e) Strong rigidity variations with depth near the megathrust interface compared to global averages L2012 (*9*) and SR2019 (*5*). For the latter comparison, we assume 4 km water depth.

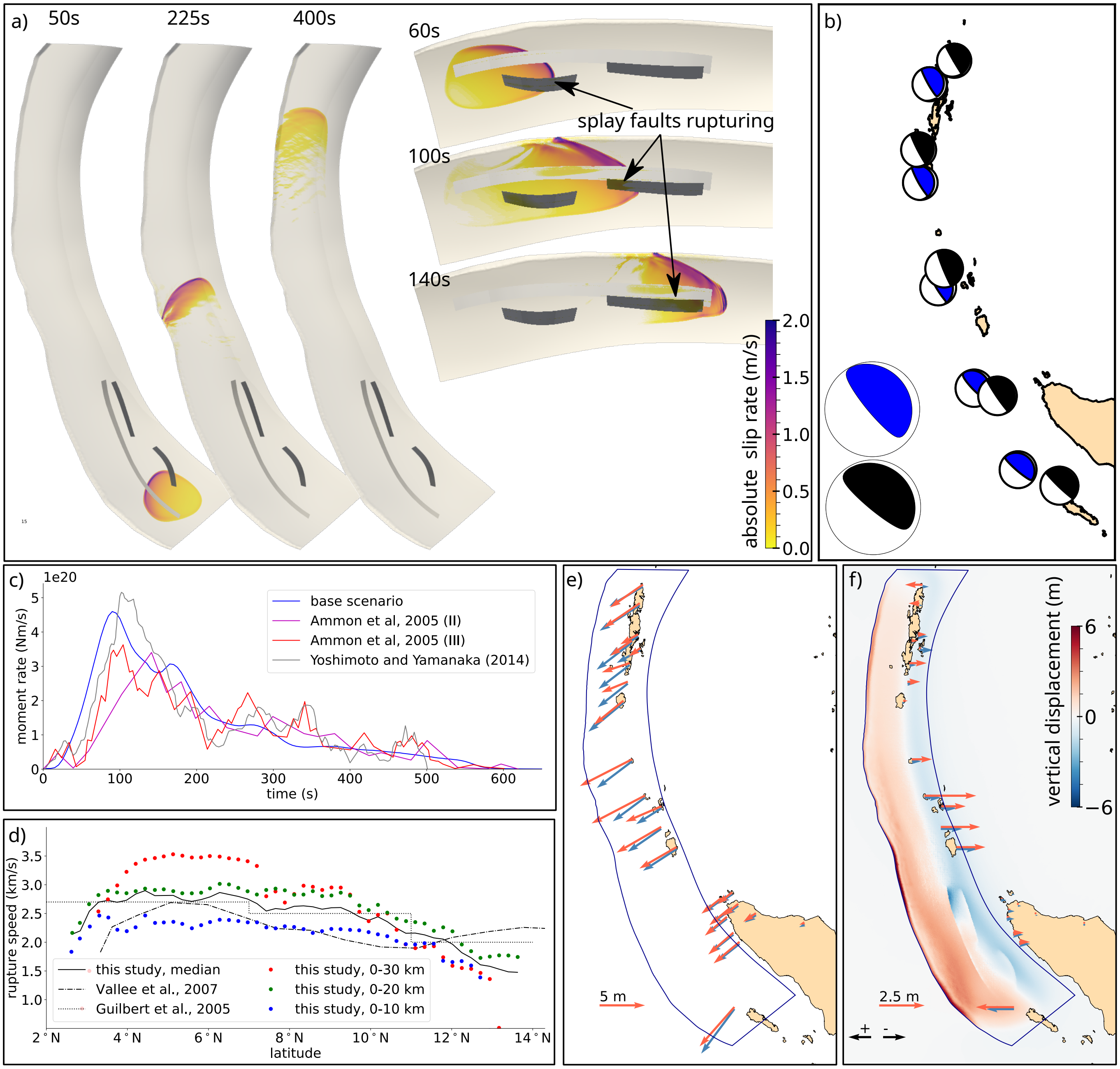

Figure 2: Dynamics and kinematics of the observational constrained dynamic rupture model of the 2004 Sumatra-Andaman earthquake. (a) Boomerang shaped megathrust slip pulse consisting of multiple rupture fronts. Snapshots of absolute fault particle velocity (slip rate). (b) Moment-tensor representation of the dynamic rupture scenario (blue, large) compared to the moment-tensor representation inferred by USGS (black, large) and comparison of a five point source model derived from the dynamic scenario (blue, small) with a respective solution from teleseismic inversion (*21*) (black, small). (c) Synthetic moment rate release compared with observational inferences from teleseismics by (*17*) (II from intermediate-period surface wave and long-period seismograms, III from teleseismic body waves, intermediate-period three-component regional waves, and long-period teleseismic waves) and (*109*). (d) Along-arc and along-depth variation of rupture speed, compared with inference from Rayleigh waves (*47*) and from acoustic observations (*48*). (e) and (f) Comparison of synthetic ground displacements (blue) and geodetic observations (orange). (e) Horizontal ground displacements. (f) Vertical ground displacements. The complete uplift and subsidence resulting from the dynamic rupture scenario (in m) is shown in red to blue including noticeable splay faulting signatures.

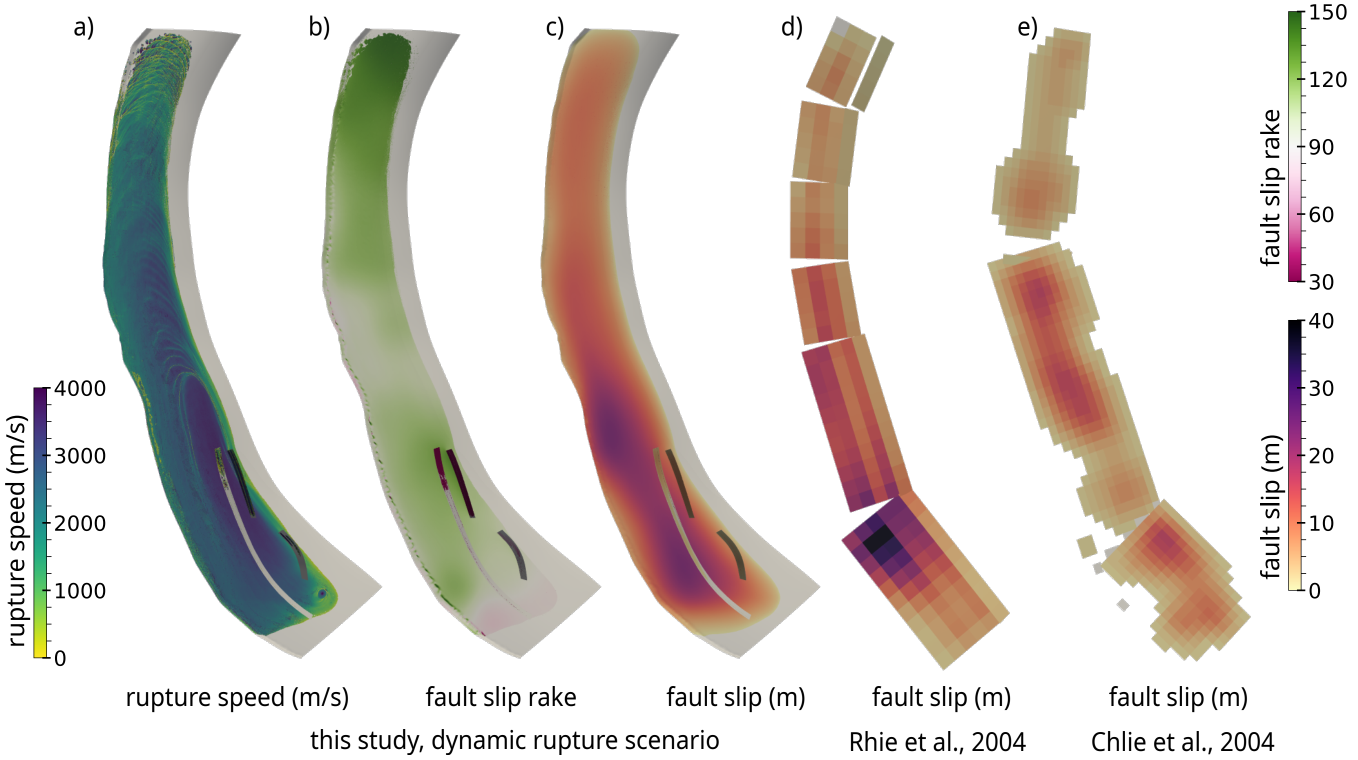

Figure 3: Source properties of the dynamic rupture scenario (a,b,c) and comparison with previously published kinematic models. (a) rupture speed, (b) fault slip rake angle, (c) fault slip, (d) kinematic slip model based on seismological and geodetic data (*19*) (e) kinematic slip model from geodetic observations (*18*).

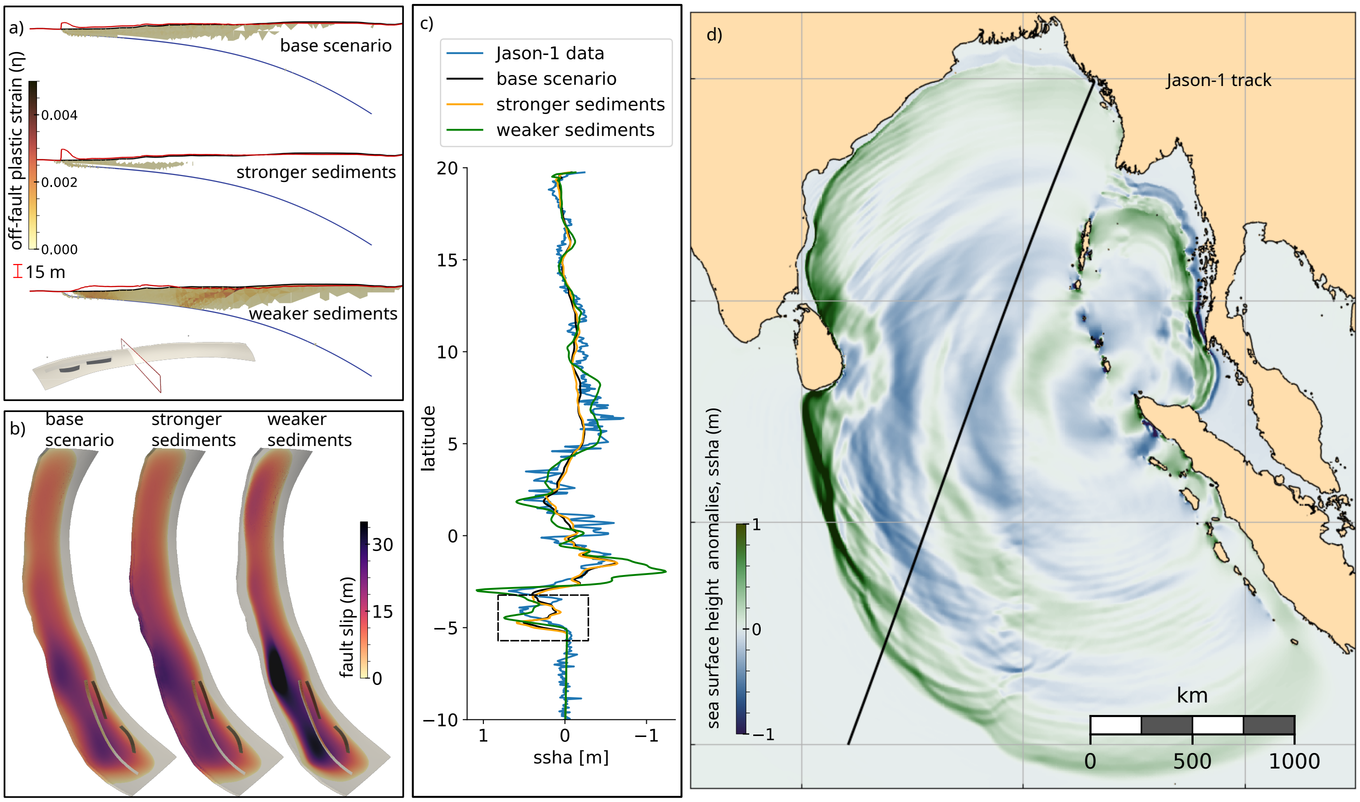

Figure 4: Off-fault yielding and tsunami genesis. a) Off-fault plastic strain (quantified as η, Eq. 10) accumulated in the base and 2 alternative earthquake scenarios with differing visco-elastic characteristics yielding stronger or weaker sediments. We use a linear scale, cut-off at $\eta > 10^{-5}$. The red line is the vertical seafloor uplift (not to scale, amplified ×200). The location of the mid-arc cross-section is illustrated beneath. Cross-sections in the South and North are shown in Fig. E4b,c b) Fault slip (m) of the three scenarios. For clarity, we use a saturated color scale for the weaker sediment scenario which has peak fault slip of 48 m). c) Tsunami induced sea surface height anomalies (ssha, m) recorded by the Jason-1 satellite about 2 hours after the mainshock compared with tsunami synthetics sourced by the three earthquake scenarios shown in (b). The dashed black rectangle highlights two short period peaks of the first tsunami wave captured by all scenarios. d) Snapshot of the tsunami simulation sourced by the base dynamic rupture earthquake scenario at 2 hours simulation time and Jason-1 satellite track.

EXTENDED DATA

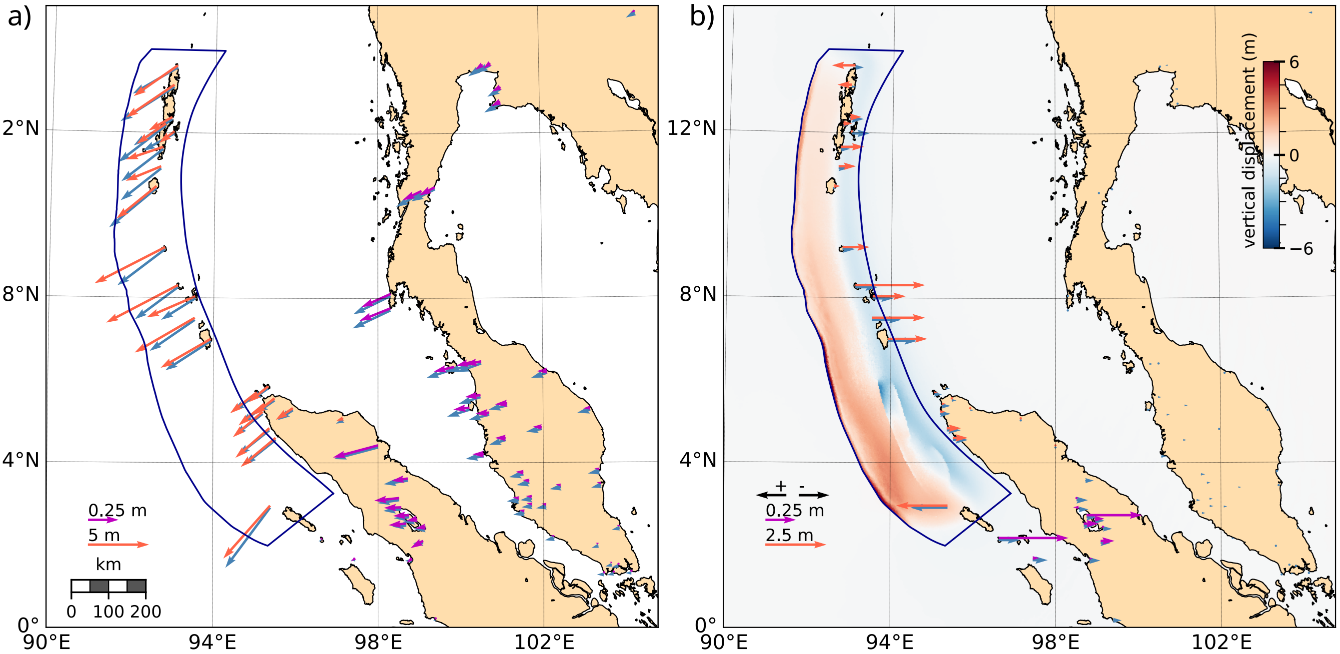

Figure E1: Comparison of synthetic ground displacements (blue) and geodetic observations (orange and magenta). In the far-field a different scaling is applied. (a) Horizontal ground displacements. (b) Vertical ground displacements. The complete uplift and subsidence resulting from the dynamic rupture scenario (in m) is shown in red to blue including noticeable splay faulting signatures.

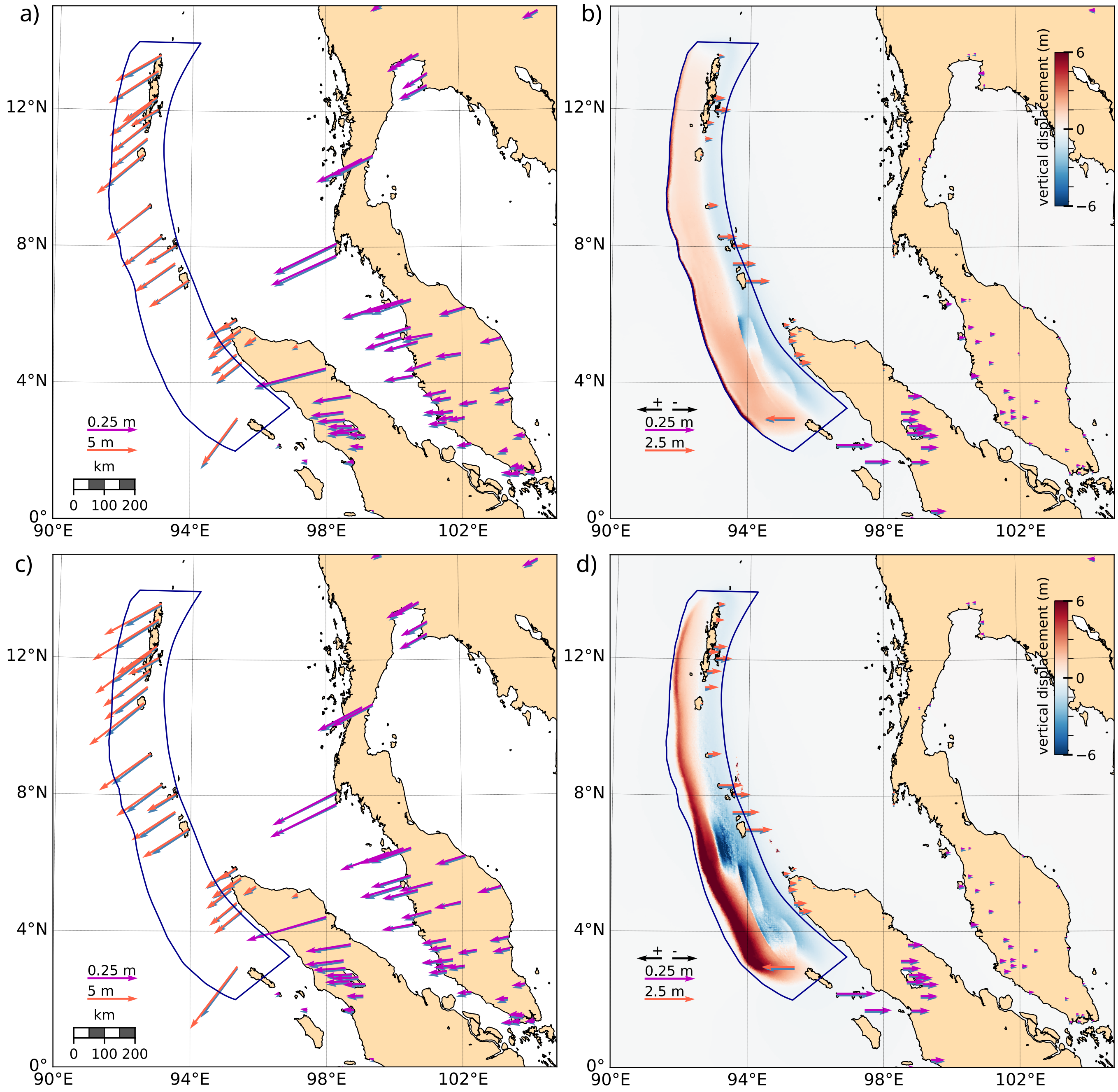

Figure E2: Comparison of synthetic ground displacements in the base scenario and in the two scenarios with alternative visco-elastic parameters shown in Fig. 4, yielding weaker or stronger sediments. A different scaling is applied to highlight smaller scale distant ground displacements. In all panels, blue is the preferred scenario and orange (or magenta, depending on the scaling) is either the scenario with stronger (a, b) or weaker (c, d) sediments. (a,c): horizontal displacements. (b,d): vertical displacements. The distribution of vertical surface displacements of the scenario with stronger sediments is shown in red to blue in (b), and with weaker sediments in (d). Note the saturated color scale, synthetic vertical displacements range between -4.7 m and 12.4 m (-9.3 m and 14.4 m, respectively) for the scenario with stronger (weaker, respectively) sediments.

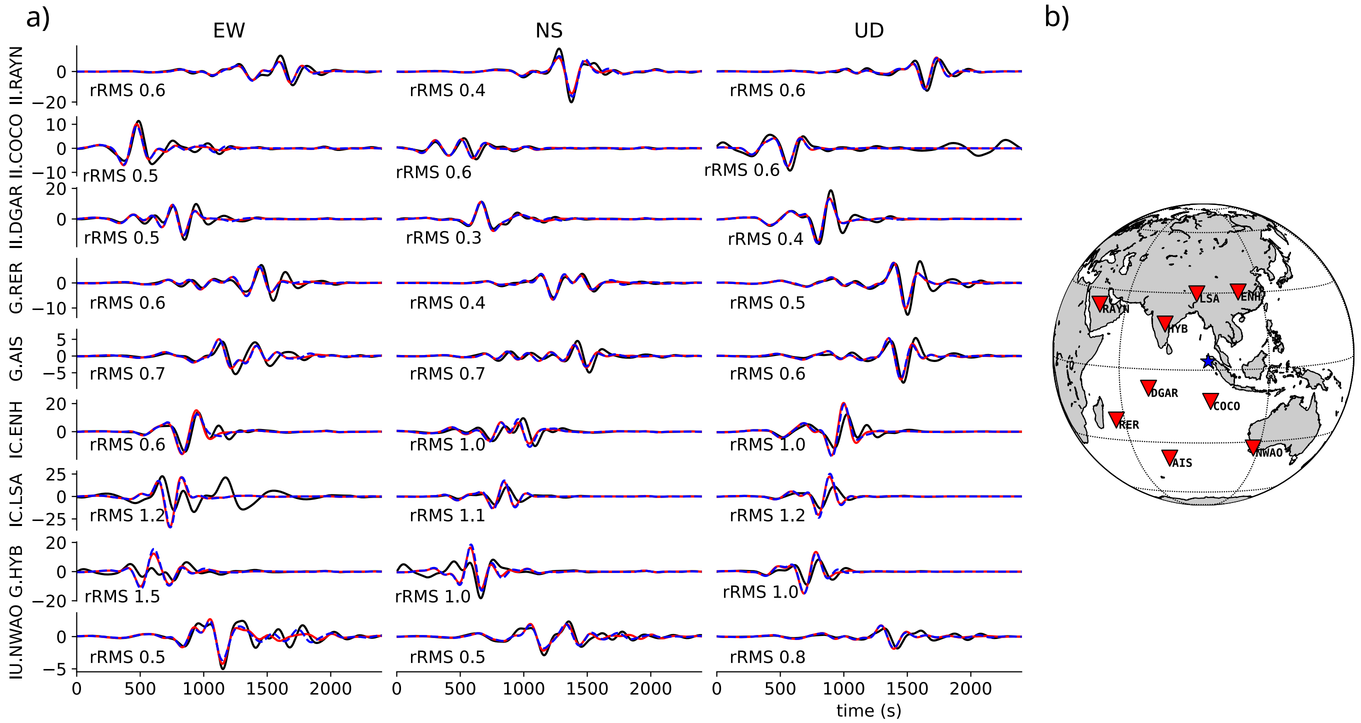

Figure E3: Teleseismic waveforms. (a) Comparison of synthetic (red and blue) and observed (black) teleseismic waveforms. Red waveforms are computed using the base scenario, while blue waveforms correspond to the model featuring less off-fault yielding and more slip to the trench, yet, indistinguishable synthetics, shown in Fig. 4. A 150-500 s band-pass filter is applied to all traces. Synthetics are generated using Instaseis (*102*) and the PREM model including anisotropic effects and a maximum period of 10 s. (b) Locations at which synthetic data are compared with observed records.

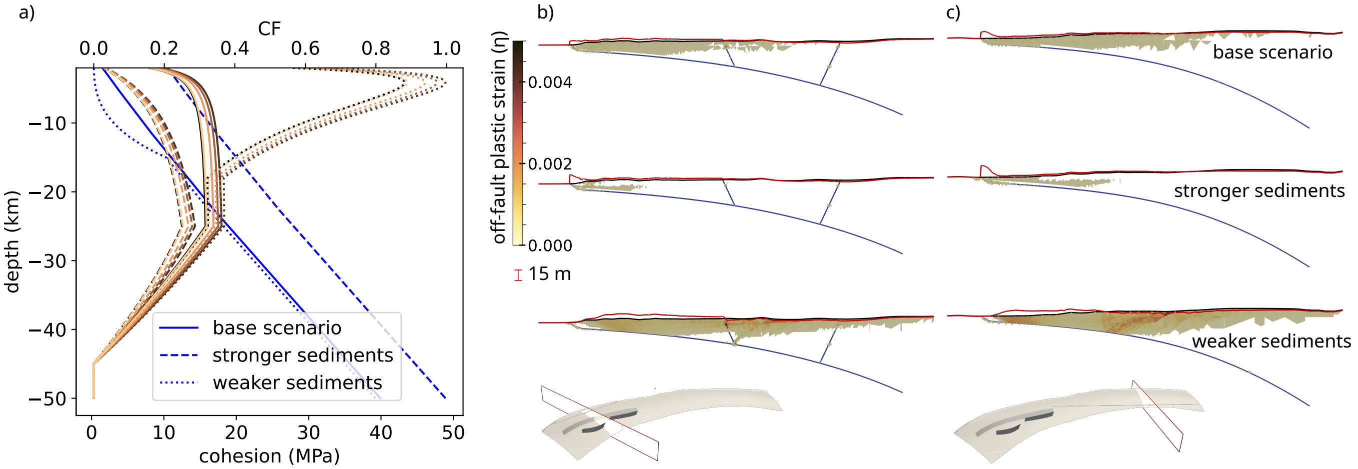

Figure E4: Off fault plasticity. (a) Depth dependence of bulk cohesion $C(z)$ (Eq. 6, blue) and of the failure criterion CF (Eq. 7, warm colors) at four locations along the trench (from south to north, the curves are colored in gold, orange, brown and black). Different line styles refer to different scenarios.(b) and (c) Off-fault plastic strain (quantified as η, Eq. 10) accumulated in the base and 2 alternative earthquake scenarios with differing visco-elastic characteristics yielding stronger or weaker sediments. We use a linear scale, cut-off at $\eta > 10^{-5}$. The red line is the vertical seafloor uplift (not to scale, amplified ×200). The locations of the southern (b) and northern (c) cross-sections are illustrated beneath. The distribution of η across the central rupture region is shown in the main text Fig. 4a.

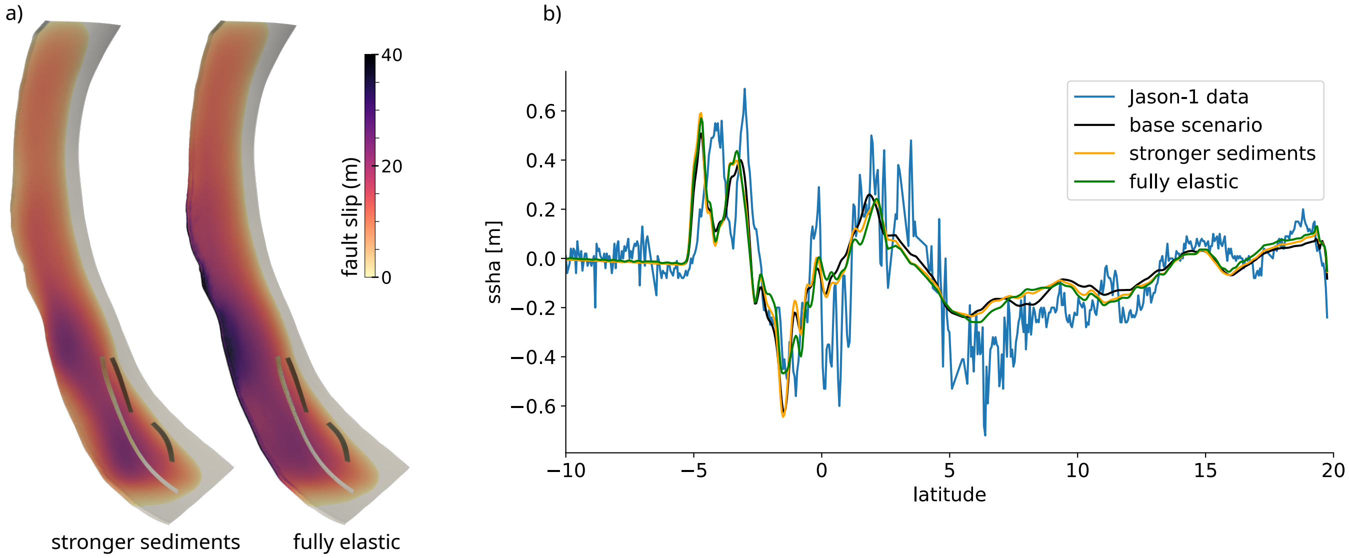

Figure E5: (a) Fault slip of the stronger sediments scenario compared to a fully elastic scenario. Note that the color scale saturates for the fully-elastic scenario which has a maximum fault slip of 52 m near the trench. (b) Sea surface height anomaly (blue, ssha (m)), recorded by the Jason-1 satellite about 2 hours after the mainshock compared with tsunami synthetics dynamically sourced by the base (black), stronger sediments (orange), and fully-elastic scenario (green).

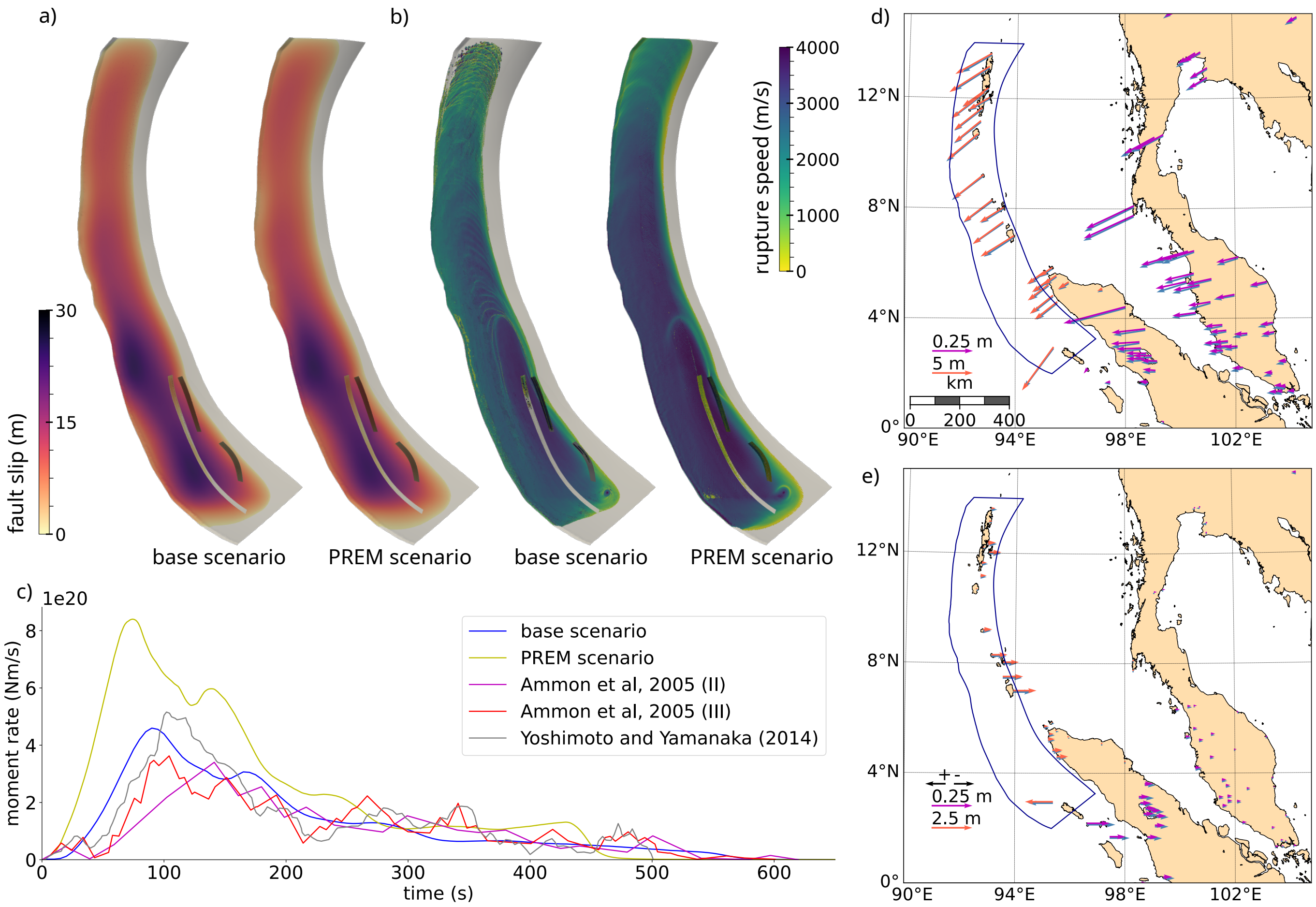

Figure E6: (a) Fault slip and (b) rupture speed of the base scenario (left) and of the alternative dynamic rupture scenario based on a PREM model ((*72*), right). Slip rates of the PREM model are provided as supplementary animation (Sumatra_SR_base_PREM.mp4). (c) Synthetic moment rate release of the PREM earthquake scenario compared with the base scenario and observational inferences from teleseismic data. (d),(e) Comparison of synthetic horizontal (d) and vertical (e) ground displacements (blue: base scenario, orange and magenta: PREM scenario). Note the different scaling applied in the far-field.

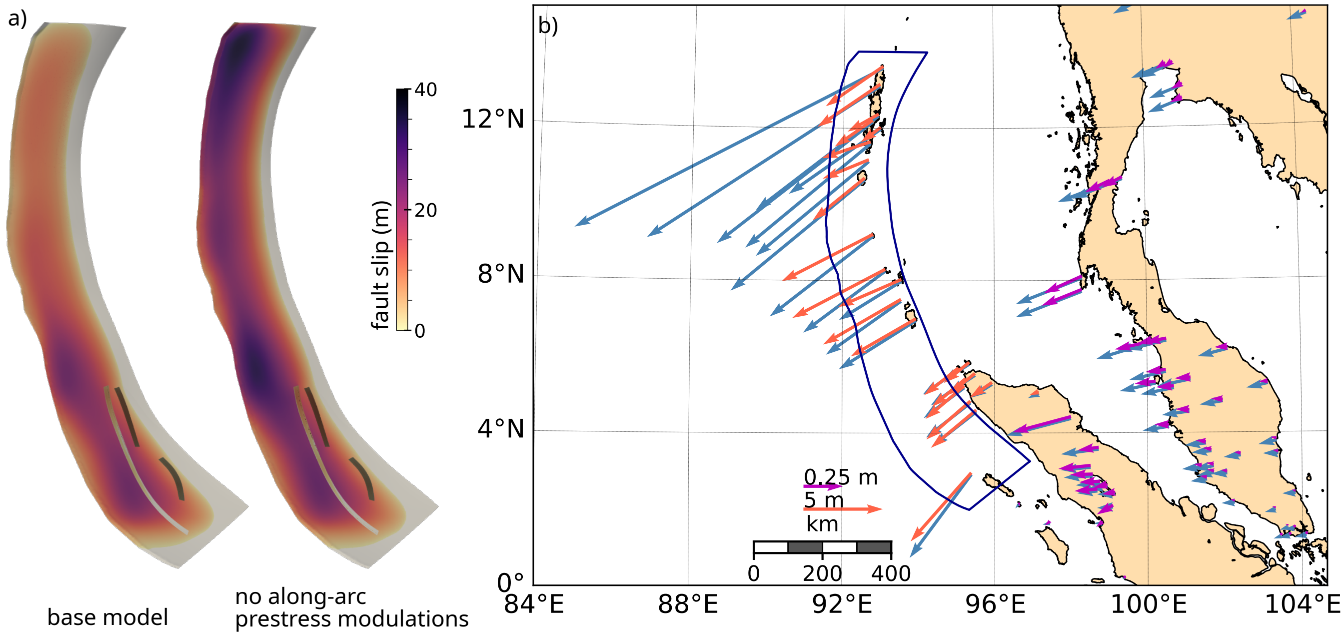

Figure E7: (a) Fault slip of the base scenario (left) and alternative scenario without regional along-arc prestress modulation (right). (b) Comparison of synthetic horizontal ground displacements (blue: scenario without along-arc prestress modulations), orange and magenta: geodetic observations). Note the different scaling applied in the far-field.

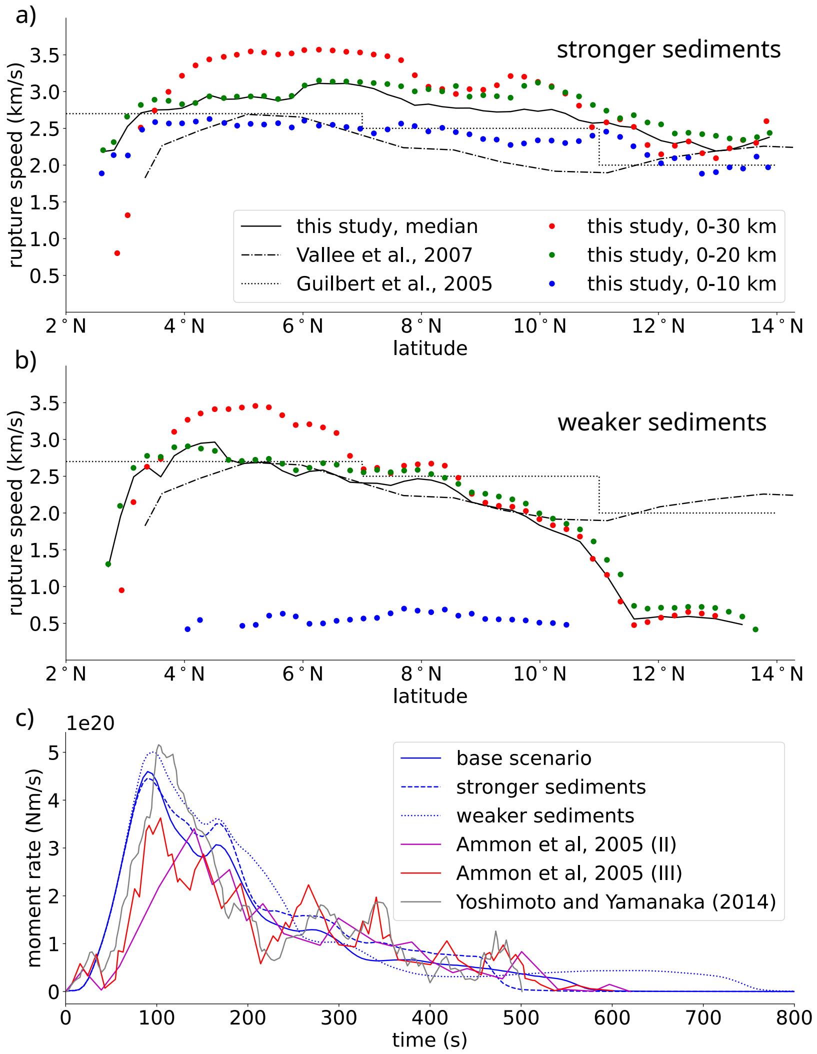

Figure E8: Sensitivity of rupture speed and moment rate release with respect to the strength of near-fault sediments. (a),(b) Along arc-variation of rupture velocity of two scenarios yielding stronger (a) or weaker (b) sediments compared to observational inferences from Rayleigh (*47*) and acoustic waves (*48*). (c) Comparison of moment rate release of the base scenario, two scenarios yielding weaker or stronger sediments and observational inferences from teleseismics (*17, 109*).

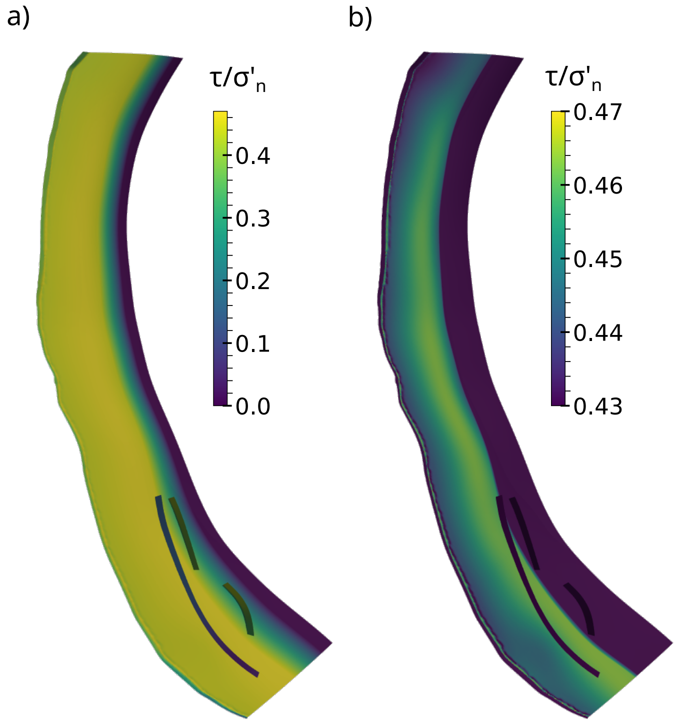

Figure E9: Ratio of initial shear stress τ over effective normal stress σ'_n. (a) τ/σ'_n distribution plotted with a colormap covering the whole range of variation of τ/σ'_n. (b) τ/σ'_n distribution plotted over a much narrower colormap range, highlighting the (limited) variation of τ/σ'_n across the earthquake rupture area.

Table E1: Contribution of plastic moment to the total seismic moment in the base scenario and the two scenario designed with alternative visco-elastic parameters as shown in Fig. 4, yielding weaker or stronger sediments. $M_{0,\mathrm{p}}$: seismic moment due to off-fault plastic strain, $M_{\mathrm{w,p}}$: seismic moment magnitude corresponding to $M_{0,\mathrm{p}}$, $M_{0,\mathrm{e}}$ seismic moment due to slip on the fault, $M_{\mathrm{w,e}}$: seismic moment magnitude corresponding to $M_{0,\mathrm{e}}$, $M_{0,\mathrm{t}} = M_{0,\mathrm{e}} + M_{0,\mathrm{p}}$: total seismic moment, $M_{\mathrm{w,t}}$: total seismic moment magnitude.

	$M_{0,\mathrm{p}}$ (Nm)	$M_{\mathrm{w,p}}$	$M_{0,\mathrm{e}}$ (Nm)	$M_{\mathrm{w,e}}$	$M_{0,\mathrm{p}}/M_{0,\mathrm{e}}$	$M_{0,\mathrm{p}}/M_{0,\mathrm{t}}$	$M_{0,\mathrm{t}}$
Base scenario	8.744×10^{20}	7.89	7.840×10^{22}	9.19	1.12%	1.10%	9.20
stronger sediments scenario	2.658×10^{20}	7.55	8.575×10^{22}	9.22	0.31%	0.31%	9.22
weaker sediments scenario	6.972×10^{21}	8.49	8.551×10^{22}	9.22	8.15%	7.54%	9.24

Supplementary Information

Earthquake nucleation

The model earthquake hypocenter is set to 30 km depth at the modeled subduction interface closest to the location inferred by USGS (3.316°N, 95.854°E). A smooth nucleation process is achieved by reducing the friction coefficient from its static to its dynamic value over 0.5 s within a spherical zone surrounding the hypocenter. The forced nucleation area expands at variable speed (maximum 2660 m/s) (*92*) to a maximum radius of 10.0 km. We decrease D_c in the hypocentral region to 1.0 m, which allows for a smaller nucleation area. D_c transitions linearly to its larger value of $D_c = 2.5$ m over 60 km (Fig.1a), which may reflect hierarchical rupture growth (e.g., (*110*)).

3D velocity model

To ensure reproducibility, we here further detail the 3D velocity model of the Sumatra-Andaman region that we summarize in Methods Sec.“Regional lithological structure”.

The model is based on a global model of the crust compiled from geologic and geophysical data (Crust 1.0 (*69*)) and is refined in the subduction region to be geometrically compatible with the subduction interface. We first partition the computational domain into 2 regions using the subduction interface geometry, described in Methods Sec. “Fault geometry”. For the oceanic crust, from the west of the model to the trench, we incorporate the (smoothed) geometry of the 3 deepest layers of the crustal model (*69*). These layers resemble a subducted crust and are thus bent downwards parallel to the subduction interface from the trench without intersecting it. We constrain the minimum distance between each layer and the megathrust to be 2.5, 5, and 14 km, respectively. Each layer is assigned average elastic parameters of Crust 1.0 as detailed in Table S1. For the continental crust, we assume a layered 1D velocity structure as detailed in Table S1. We constrain layer thickness and elasticity parameters from crustal tomography of the continental crust beneath the Andaman Island by (*111*).

Megathrust and splay fault geometry

Incorporating realistic fault geometries is important for dynamic rupture models driven by regional tectonic loading, as the fault geometry modulates the on-fault normal and shear tractions and therefore the rupture process. In particular, the steepness of the slab interface plays a major role in modulating synthetic ground displacements (*64*). We adopt the slab interface from Slab 2.0 (*73*), which assembles 3D geometries of most megathrust interfaces, constrained by seismological and geophysical observation (e.g. CMT solutions, active seismic profiles). Slab 2.0 shows that the Sunda megathrust smoothly steepens from the trench to deeper depths.

We allow for shallow dynamic rupture in our model by intersecting the subduction interface geometry with the bathymetry and topography of the ground surface. The shallowest part of the Slab 2.0 geometry, located 2 to 5 km below the seafloor, is mostly horizontal. Surface rupture during the 2004 event may have occurred on a shallow thrust fault splaying from the slab interface within the accretionary wedge, as suggested from inferred shallow patches of large fault slip (e.g., (*112*)). Surface rupture in our model is enabled by incorporating a short splay fault at the tip of the subduction interface, smoothly connected with the subduction interface. This short splay dips at 30° near the seafloor and intersects with the bathymetry at the trench. At depth it smoothly connects with the subduction interface.

Model resolution

The structural model is discretized into a computational mesh consisting of 20 million elements. Geometric resolution is set to $h = 1$ km across all faults and the mesh is coarsened away from the fault system but at maximum twice the S-wave velocity of each respective layer. In the subduction channel we enforce a mesh size of 2 km or less. We choose polynomial basis functions of order $p = 4$ leading to a 5^{th} order accurate numerical scheme in space and time. In Seissol, each dynamic rupture element face is discretized by $(p + 2)^2$ Gauss points, enabling sub-elemental resolution of rupture dynamics. The simulations we present can be executed using either small-scale computational resources (e.g. institute / university resources, run-times being 30h on 10 nodes) or large-scale national computational facilities (with run-times 3h on 120 nodes). As an illustration, simulating 900 s of dynamic rupture and wave propagation requires 3 h on 5760 Intel Skylake cores of the supercomputer SuperMucNG (Leibniz Supercomputing Center, Germany).

The process zone width Λ (*113*) defined as the area behind the rupture front in which shear stress decreases from its static to its dynamic value, determines numerical convergence on the faults. In the preferred dynamic rupture scenario, the median Λ is about 6 km, while 95% of the ruptured fault elements have Λ greater than 2.5 km. The model adequately resolves Λ with at least 2.5 elements and polynomial basis functions of order $p = 4$ (see the detailed h/p refinement analysis in (*89*)).

We here use a relatively coarse discretization compared with high-resolution dynamic rupture models on segmented crustal fault networks (e.g., (*43*)), due to the large process zone width and smooth geometry of the subduction interface and splay faults.

Multiple point source analysis: source time functions

In Fig. S1, we evaluate the dynamics of the base earthquake scenario in comparison to the 5 point source kinematic model of (*21*), which is inferred from teleseismic data. The synthetic moment released in our scenario is derived from the slip across all faults of the dynamic rupture scenario.

The source time function amplitudes are smaller than in (*21*), except for the first point source. This may reflect the overall discrepancy in moment magnitude which is 9.2 in our scenario compared to 9.3 in (*21*). The moment modeled here falls well within the range of uncertainties in observational estimates ranging from M_w 9.1 to 9.3 (*26*) attributed to trade-offs between the inferred seismic moment and assumed fault dip and other near-source properties.

Supplementary Movies

We provide several animations illustrating the earthquake and tsunami scenarios at `https://syncandshare.lrz.de/getlink/fiT4a9XQmausR5TE47GqB4GT/`.

Sumatra_SR_base_stronger_weaker.mp4 is an animation showing the rupture dynamics of three earthquake scenarios discussed, in terms of absolute slip rate (m) across the fault network, side by side (left: base, middle: stronger sediments, right: weaker sediments scenario). Sumatra_SR_base_PREM.mp4 is an animation showing the rupture dynamics of the base and PREM earthquake scenarios, in terms of absolute slip rate (m) across the fault network, side by side (left: base, right: PREM scenario). In addition, Sumatra_SR_base.mp4 and Sumatra_SR_stronger.mp4 and Sumatra_SR_weaker.mp4 show animations of each individual scenario.

We also provide animations of the tsunami scenarios associated with the three earthquake scenarios discussed: base (tsunamiBaseScenario.mp4), stronger sediments (tsunamiStrongerSediments.mp4) and weaker sediments (tsunamiWeakerSediments.mp4) scenarios. The tsunami animations show the evolution of the sea surface height amplitudes (in meter) as predicted by each tsunami scenario.

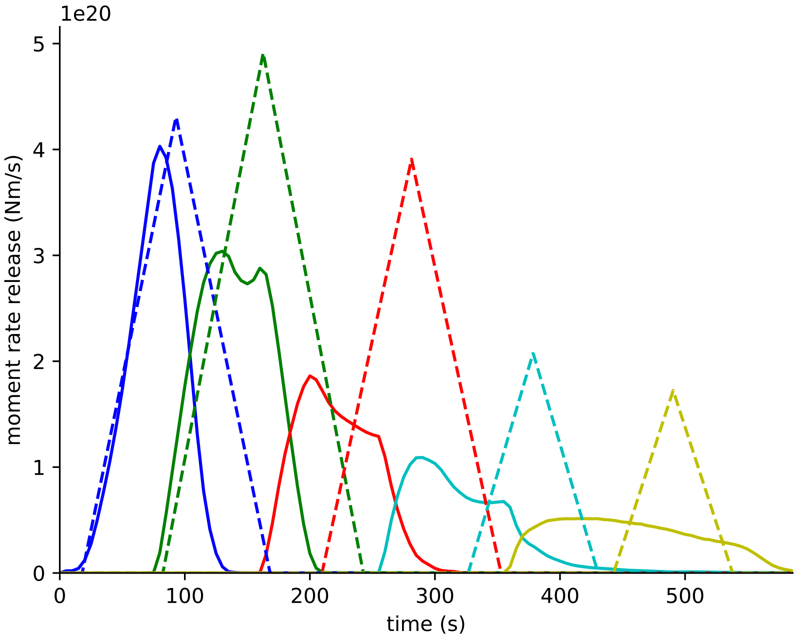

Figure S1: Comparison of the 5 point-source model derived from the preferred dynamic rupture scenario and Tsai et al.'s (*21*) teleseismic inversion: Moment rate release of each point source. Dashed line: Tsai et al. (*21*), solid line: dynamic rupture scenario. From south to north, moment rate release time series are colored in blue, green, red, cyan and yellow.

Table S1: Elastic parameters assumed in the 3D velocity model. ρ, μ, λ, V_p and V_s are respectively the density, the Lamé parameters and the P- and S-wave velocities. Note that we here report the maximum and minimum material properties in the subduction channel (SC), enclosing the subduction interface. Their detailed distribution with 1 km resolution are provided in the files (Sumatra_rhomulambda.yaml). Within the continental crust, a 1D layered model is used.

	lower depth (km)	ρ (kg/m^3)	μ (MPa)	λ (MPa)	V_p (m/s)	V_s (m/s)
Continental 1	6	2550	15.94	15.27	4300	2500
Continental 2	20	2720	33.32	31.28	6000	3500
Continental 3	∞	3300	65.94	81.23	8000	4450
SC min	0	2245	5.06	11.46	3100	1500
SC max	∞	2887	43.13	43.73	6700	3900
Oceanic 1	meshed	2500	22.50	27.90	5400	3000
Oceanic 2	meshed	2850	39.02	42.38	6500	3700
Oceanic 3	meshed	3050	50.03	53.70	7100	4050
Oceanic 4	meshed	3330	65.94	81.24	8000	4450